Theoretical modelling and observational study of supernovae model with self-consistent solutions to radiative transfer equations in an expanding shell

A thesis
Submitted towards the partial fullfilment of
BS-MS dual degree programme
by

Vishal Ravishankar

Date:May 19 2023

under the guidance of

Firoza Sutaria

Indian Institute of Astrophysics

from June 2022 to May 2023

Indian Institute of Science Education and Research
Pune

Certificate

This is to certify that this dissertation entitled "Theoretical modelling and observational study of supernovae model with self-consistent solutions to radiative transfer equations in an expanding shell" submitted towards the partial fulfillment of the BS-MS degree at the Indian Institute of Science Education and Research, Pune represents original research carried out by Vishal Ravishankar at Indian Institute of Astrophysics, under the supervision of Firoza Sutaria during academic year June 2022 to May 2023.

Supervisor:
Firoza Sutaria
Associate Professor
Indian Institute of
Astrophysics

Vishal Ravishankar
20181114
BS-MS
IISER Pune

Date:
19/05/2023

Declaration

I, hereby declare that the matter embodied in the report titled "Theoretical modelling and observational study of supernovae model with self-consistent solutions to radiative transfer equations in an expanding shell" is the results of the investigations carried out by me at the Indian Institute of Astrophysics from the period 01-06-2022 to 19-05-2023 under the supervision of Firoza Sutaria and the same has not been submitted elsewhere for any other degree.

Supervisor:
Firoza Sutaria
Associate Professor
Indian Institute of
Astrophysics

Vishal Ravishankar
20181114
BS-MS
IISER Pune

Date:
19/05/2023

Acknowledgements

I would like to express my deepest gratitude to the following individuals and organizations who have supported me throughout the process of completing this thesis:

First and foremost, I would like to thank my thesis supervisor, Firoza Sutaria. Her guidance and support were invaluable to me throughout the entire year. She generously offered her time to have discussions with me frequently.

I would also like to extend my sincere appreciation to Anish Parwage, who provided me with tremendous help and guidance with NOVA, a high-performance computing cluster. He also assisted me in setting up MESA, a stellar evolution code, and SNEC, a supernova explosion code. His expertise and patience were invaluable to me.

I am grateful to the IIA support team for their prompt assistance with Wi-Fi and computer issues, which were essential to the success of my research. I owe a great debt of gratitude to Prasad Subramanian, my thesis expert, for facilitating my thesis so well. His insights and guidance were invaluable in shaping my work. I would also like to thank Arun Thallapillil, my supervisor on my previous semester projects. His assistance in helping me figure out what I wanted to pursue was invaluable.

I would also like to thank the Indian Institute of Science Education and Research (IISER) Pune, where I am currently a student, for their support and encouragement throughout my academic journey.

Additionally, I would like to acknowledge the Astropy development team, the SNEC developers, the MESA support teams, and the SNID and AstroDASH developers for providing invaluable resources and tools for my research.

I am grateful to the team behind ATLAS forced photometry server, which is publicly accessible, for providing me with the necessary data for my research

Finally, I would like to thank my family and friends for their unwavering support and encouragement throughout this process. Their belief in me has been a constant source of inspiration.

Abstract

Core-collapse supernovae events are classified among various sub-types, mainly determined by the extent and composition of the outermost layers of the progenitor, as well the circumstellar medium (CSM). However, with the advent of optical transient "factories" in the last decade or so, it has become clear that there is a considerable diversity even among the various subtypes, and that "cross-over" events (e.g. type-IIP to type-L etc.), which transition from one subtype to another during their temporal evolution, are more common than was previously believed. Thus, one aim of this MS thesis project was to look at recent spectroscopic observations and light curves of core-collapse SNe to find esoteric sub-classes. One such sub-class is FBOTs

The Fast Blue Optical Transient (FBOT) AT 2022kmm has a light curve as bright as superluminous supernovae but rises and falls much faster. We reproduced this light curve using 2 models: circumstellar interaction of a pulsational pair-instability supernova (PPISN) model and 15 M ZAMS mass star that has been evolved to core-collapse that has experienced different extent of hydrogen envelop stripping

Mass loss and progenitor properties from massive stars being as yet modelled, such a work provides a direct estimate of the nature of the CSM, and the post-main sequence (post-MS) epoch at which it was created. The lightcurve will be modelled using SNEC, publicly available codes. Once the composition and the epoch of the CSM creation are modelled, we used MESA a stellar evolution code (with mass-loss introduced to account for CSM generation) to track the post-MS evolution of the progenitor star.

Contents

List of Figures

List of Tables

Chapter 1

Introduction

1.1 Understanding theory of Supernova :

After the initial collapse and formation of a proto-neutron star, matter accretion hitting the surface of the neutron star creates the initial shock wave. As this shock wave propagates through a heavy nuclei medium, it dissociates the nuclei into nucleons. The electron capture rate on the free protons is significantly larger on the neutron-rich nuclei. As a result, a large fraction of the neutrinos produced by these electron captures leave the star quickly in what is known as a neutrino burst.

The shock wave eventually weakens and stalls, turning into an accretion shock. The matter downstream of the shock has a negative velocity and continues to fall inward. The stalled shock wave is then revived by the neutrinos streaming off the neutrino-sphere through a process known as neutrino heating. This is a self-enhancing effect whereby the strong heating of matter accreted by the shock decelerates the infall and increases the time for the matter to absorb neutrino energy, thereby raising the efficiency of the energy deposition by neutrinos.

The neutrino heating forms a hot bubble region that increases the pressure behind the shock, causing the heated layers to expand. This creates a region of low density and high temperature between the shock front and the proto-neutron star surface. A negative entropy gradient behind the accretion shock is generated because the neutrino heating is much stronger near the gain radius[1] than at larger distances from the neutrino-sphere.

[1]Gain radius: the position where the neutrino heating rate per nucleon and the neutrino cooling rate per nucleon becomes equal

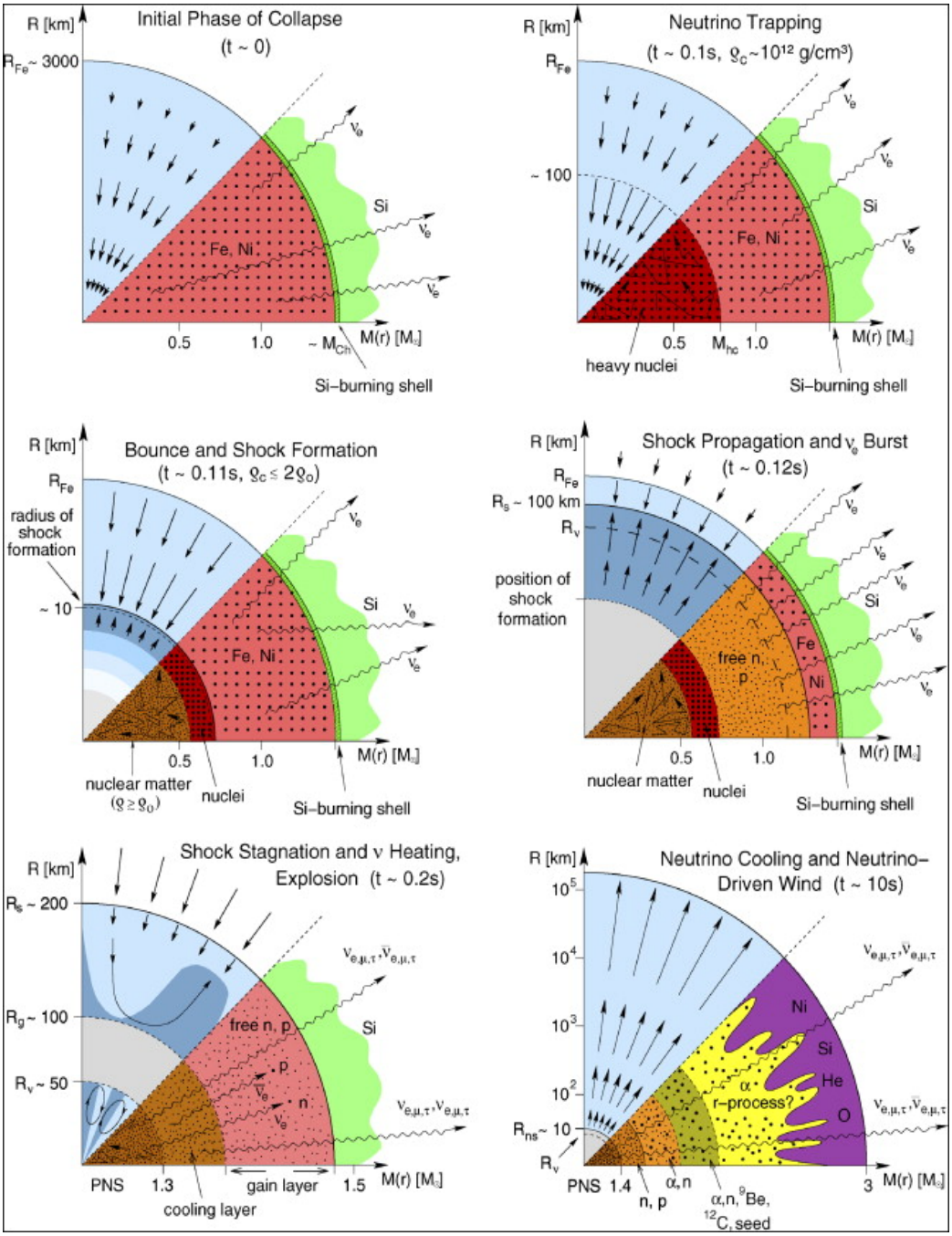

Figure 1.1: The schematics track the evolution of the progenitor star's core and outer layers, starting at the epoch of collapse (time t=0.0 s), and ending at t=10s, when the shocked-out layers are ejected from the epicenter of the explosion. Figure is taken from "Theory of Core-Collapse Supernovae" *Janka,H. et al. (2006)*

Six phases of neutrino production and its dynamical consequences (from top left to bottom right). In the lower halves of the plots, the composition of the stellar medium and the neutrino effects are sketched, while in the upper halves, the flow of the stellar matter is shown by arrows. Inward-pointing arrows denote contraction or collapse, outward pointing arrows expansion or mass ejection. Radial distances R are indicated on the vertical axes, and the corresponding enclosed masses $M(r)$ are given on the horizontal axes. R_{Fe}, R_S, R_ν, R_g, and R_{ns} denote the iron-core radius, shock radius, neutrinospheric radius, gain radius (which separates neutrino cooling and heating layers), and proto-neutron star (PNS) radius, respectively. M_{Ch} defines the effective Chandrasekhar mass, M_{hc} the mass of the homologously collapsing inner core (where velocity $u \propto r$), ρ_C the central density, and $\rho_0 \approx 2.7 \times 10^{14}$ g cm^{-3} the nuclear saturation density.

1.2 Light curve of a supernova

The light curve of a supernova can be explained by the interplay of different physical processes that occur during the explosion. One of the main mechanisms responsible for the initial rise of the light curve is the shock breakout. During the supernova explosion, a shockwave is generated that travels outward from the collapsing core and breaks out of the stellar envelope. The energy released by the shock causes a sudden increase in the luminosity of the supernova, which is observed as the initial peak in the light curve.

After the shock breakout, the luminosity of the supernova is mainly determined by the cooling of the expanding ejecta. As the ejecta expands, it cools by adiabatic expansion and radiation. Initially, the ejecta is fully ionized, and most of the cooling occurs via free-bound and bound-bound transitions in the ionized atoms. This phase is known as the recombination phase, and it is responsible for the plateau in the light curve that follows the initial peak.

Eventually, the ejecta cool enough to allow the formation of neutral atoms. This phase is known as the nebular phase, and it is characterized by a rapid decline in the luminosity of the supernova. At this stage, the supernova is mainly powered by the radioactive decay of nickel-56 and cobalt-56, which were synthesized during the explosion. The energy released by the decay of these radioactive isotopes heats the ejecta and powers the emission of photons, which are observed as the late-time tail of the light curve.

In summary, the light curve of a supernova is shaped by the interplay of

different physical processes that occur during the explosion, including shock breakout, ejecta cooling via recombination, and the radioactive decay of synthesized isotopes.

SN classification:

1.3 Type I

Type I supernovae are a distinct class of supernovae that lack the characteristic hydrogen spectral lines in their spectra. They are primarily categorized based on the presence or absence of other specific spectral features, primarily lines from ionized silicon (Si II) and/or helium (He I). Type I supernovae are further divided into several subtypes, including Type Ia, Type Ib, and Type Ic, each with unique characteristics and origins.

1.3.1 Type Ia

Type Ia supernovae are an important class of stellar explosions that occur in binary star systems, where one of the stars is a white dwarf. These supernovae result from the accretion of material from a companion star onto the surface of the white dwarf, causing it to reach a critical mass and trigger a runaway nuclear fusion reaction that consumes the entire white dwarf. This explosion releases a tremendous amount of energy and creates a luminous outburst that can outshine an entire galaxy for a brief period of time.

Type Ia supernovae have become an essential tool in modern astrophysics, as they are used to measure the distances to distant galaxies and study the expansion history of the universe. This is because these supernovae are remarkably uniform in their properties i.e. characteristic light curve and a distinct silicon absorption line around 615nm, making them valuable "standard candles" for measuring cosmic distances. The underlying physics of Type Ia supernovae is complex, involving the interactions between nuclear reactions, hydrodynamics, and radiation transport, and remains an active area of research in astrophysics.
Roche Lobe Overflow: In a binary star system, the Roche lobe is the region around each star within which material is gravitationally bound to that star. When one star expands beyond its Roche lobe, material from the star can flow onto its companion. This is called Roche lobe overflow. In the case of a white dwarf and a companion star, material from the companion can flow onto the white dwarf, leading to the accretion of matter.

Accretion by White Dwarf: As material from the companion star flows onto the white dwarf, it accumulates on the surface of the white dwarf. The accretion rate can be very high, and the material can heat up to temperatures of millions of degrees, resulting in the emission of X-rays. As the accreted material builds up on the white dwarf, it can approach a critical mass known as the Chandrasekhar limit.
Pillar Formation due to Magnetic Fields: Prior to the thermonuclear runaway, the accreted material on the surface of the white dwarf can be compressed and heated by the strong gravitational field of the white dwarf. This can create a region of high pressure and temperature in the accreted material, which can trigger nuclear fusion reactions. However, for a Type 1a supernova to occur, the ignition of fusion must occur in a relatively symmetric and stable manner.
Magnetic fields can play a crucial role in stabilizing the accreted material and helping to prevent asymmetrical ignition. As the material builds up on the white dwarf, magnetic fields can become stronger, creating structures known as magnetic pillars or flux ropes. These pillars can help to channel the flow of material onto the white dwarf and stabilize the accretion process.
Thermonuclear Runaway: If the accreted material on the white dwarf exceeds the Chandrasekhar limit, it can trigger a runaway thermonuclear reaction. The energy released from the fusion reactions causes the white dwarf to rapidly heat up and expand, leading to a Type 1a supernova.
The Si II line at around 615 nm is a prominent feature in the optical spectra of Type Ia supernovae. This line is formed as a result of the explosive nuclear burning which produces Silicon among a variety of elements

1.3.2 Type Ib

Type Ib supernovae are a subclass of core-collapse supernovae that are characterized by the absence of hydrogen lines in their spectra
In Type Ib supernovae, the outer layers of the star that are ejected during the explosion have lost their hydrogen envelopes, but still contain significant amounts of helium and other elements. The absence of hydrogen lines in the spectra of Type Ib supernovae is believed to be the result of the removal of the hydrogen envelope before the supernova explosion.
The mechanism for removing the hydrogen envelope is thought to occur through a combination of stellar winds and binary interactions. The explosion of a Type Ib supernova releases an enormous amount of energy, typically equivalent to the energy output of 10^{51} erg or more. The energy released in the explosion is carried away by the ejected material, which can be observed as a bright, expanding shell of gas and dust. The ejected material also con-

tains newly synthesized heavy elements, which can be dispersed into the interstellar medium and incorporated into future generations of stars and planets.

1.3.3 Type Ic

Type Ic supernovae are a subclass of core-collapse supernovae that are characterized by the absence of both hydrogen and helium lines in their spectra SN Ib/c: after the initial shock cools radioactive heating ^{56}Ni $\rightarrow$ ^{56}Co powers the emission from the ejecta, $\sim$ 100 days ^{56}Co decay is the main source powering the light curve

Type Ic-BL (broad-line) supernovae are a subtype of core-collapse supernovae that exhibit broad absorption lines in their spectra, indicating that the ejected material is moving at extremely high velocities. The progenitor is thought to be a stripped Wolf-Rayet star, that's believed to be rapidly rotating and have strong magnetic fields, which might form the central engine which could power $\rightarrow$relativistic jet with E$\sim$ 10^{51}ergs + SN whose synthetic light curves and spectra are fully consistent with observed SN Ic-BL

Gamma-ray bursts (GRBs) are often associated with Type Ic-BL supernovae (SNe), which are thought to be the result of the collapse of massive stars. However, not all Type Ic-BL SNe are associated with GRBs, and not all GRBs are accompanied by SNe. The absence of a GRB in some cases could be due to the orientation of the GRB jet away from Earth, but other factors may also be at play.
One factor that may contribute to the association between GRBs and Type Ic-BL SNe is that the GRB jet can increase the kinetic energy of the ejecta, resulting in higher photospheric velocities and broader spectral features. In contrast, Type Ic-BL SNe without a coincident GRB typically has lower energy and narrower spectral features.
Another possible factor is the presence of a rapidly rotating progenitor star, which may allow for the formation of both GRBs and high-velocity SNe. Finally, the jet produced by the GRB could induce an asymmetric explosion, resulting in an aspherical explosion and broader spectral features in the resulting Type Ic-BL SN. The study of GRBs and Type Ic-BL SNe is an active area of research in astrophysics, with ongoing efforts to better understand the complex processes that give rise to these phenomena.
Magnetar spin-down is proposed as the kinetic energy source of SNe Ic-BL
SN shows a triple-peaked light curve and a late (re-) brightening, multi-peaked Type Ib SN

No narrow lines, extended CSM structure is seen through radio
Interaction of supernova ejecta with spherically-asymmetric CSM(disk-like) geometry of mass loss may be affected by tertiary stellar companion

1.4 Type II

Type II(H lines present)
Type II supernovae are a subtype of core-collapse supernovae that arise from the explosive death of massive stars. They are classified based on their light curves, which describe the brightness of the supernova over time. There are several subtypes of Type II supernovae, including Type II-L and Type II-P.

1.4.1 Type II-L

Type II-L supernovae are characterized by a rapid decline in their light curves, with the brightness dropping by a factor of 2 within about 100 days after the explosion. They are thought to arise from the explosion of stars with a low-mass hydrogen envelope, which is quickly ejected from the star during the explosion. As a result, the supernova lacks the hydrogen lines that are typically seen in Type II-P supernovae.

1.4.2 Type II-P

Type II-P supernovae, on the other hand, exhibit a plateau in their light curves, with the brightness remaining nearly constant for about 100 days before declining. This plateau is thought to arise from the interaction of the expanding supernova ejecta with a dense circumstellar medium, which slows down the ejecta and produces a prolonged emission of radiation. Type II-P supernovae are believed to arise from stars with a higher-mass hydrogen envelope, which is not fully ejected during the explosion.

The notations n and BL for narrow and broad lines Narrow lines in supernova spectra are typically associated with the interstellar medium and indicate the presence of low-density gas that has not been affected by the supernova explosion. Broad lines, on the other hand, are produced by the supernova ejecta and indicate the presence of high-density, rapidly expanding material.

Type IIb supernovae are a subtype of core-collapse supernovae that exhibit features of both Type II and Type Ib supernovae: spectrum initially with H lines but absent in later spectra. They are believed to arise from the explosion of stars with an initial mass of about 10-30 solar masses, which have lost most of their hydrogen envelopes prior to the explosion. This partial loss of the hydrogen envelope leads to the presence of helium lines in the supernova spectrum, similar to Type Ib supernovae.
Interaction between SN ejecta and Circumstellar medium(CSM) is stimulated to explain the observed light curve and spectrum features

1.5 SLSN

A superluminous supernova (SLSN) is a type of extremely bright and energetic explosion that occurs when a massive star reaches the end of its life and collapses under the force of gravity. While typical supernovae release an enormous amount of energy, SLSNe are much more powerful, with luminosities that can be up to several hundred times greater than that of a standard Type Ia supernova
Possible models: Pair instability SN, the interaction between SN ejecta and dense circumstellar medium(CSM), or engine driven explosion(maybe be a proto magnetar radiating enormous power during its spin down process)

1.6 Ca-rich SNe (rapidly evolving transient)

Ca-rich SNe faint, rapidly evolving transients with [CaII] emission features in their nebular phase spectra, relatively short rise and decline times. Usually detected in old stellar environments in the far outskirts of their host galaxies. Suggesting that they originate from old progenitors that have traveled a great distance from their birth site, the exact progenitor system remains unknown. γ-ray escape time of Ca-rich SNe sample is 35-65 days, within the unoccupied region between Type Ia SNe and stripped-envelope SNe. Helium shell detonation models core-collapse of ultra-stripped-unlikely(γ-rays escape time in these models is smaller than the observed values)
Interaction of He-rich hybrid 0.69 $M_\odot$ HeCO white dwarf with a more massive 0.8 $M_\odot$ CO white dwarf just before they merge, accretion from hybrid WD to CO white dwarf $\rightarrow$ Helium detonation $\rightarrow$ full detonation and disruption of the hybrid white dwarf with low $Ni^{56}(0.018M_\odot)$.

1.7 Presupernova Evolution

The mass loss of a star depends on several factors. The initial mass of the star is a key factor, with higher-mass stars having shorter lifespans, radiating more energy, and driving more winds that expel greater mass.

The metallicity of the star also plays a role, as winds of luminous hot stars are driven by absorption in the spectral lines. However, H and He are by far the most abundant elements and their impact on the wind driving is modest. It is relatively less abundant complex atoms that are the main contributors.

Rotation and binary companions can also lead to mass loss. Roche lobe overflow is a common mechanism in binary systems. Continuum-driven mass loss and envelope instabilities are other factors that can contribute.

The end-stage instability of a star can also cause mass loss. For example, precursor emission from a supernova can occur weeks to months prior to the explosion, with a single mass-loss event known as an "eruption" accompanying the interacting supernova. The luminosities of the observed precursors are well above the Eddington limit for typical supernova progenitor stars of mass 10-20 $M_{\odot}$, and this emission phase is accompanied by substantial mass-loss.

Finally, the density profile of $1/r^2$ is a consequence of continuous constant mass loss in the form of wind. When an equal amount of material is ejected by the star at the same speed, the medium's density is proportional to $1/r^2$.

Supernova subclass of the main interest of this work:

1.8 Fast Blue Optical Transient

The Fast Blue Optical Transient (FBOT) is a type of transient with a light curve as bright as superluminous supernovae but rises and falls much faster. A high-energy astrophysical phenomenon, which is believed to be a form of supernova, is responsible for this occurrence. However, its cause remains unknown, and it is thought to happen at a rate of no more than 0.1% compared to the typical rate. These transients are characterized by their ejected envelopes with a mass of $M_{ej} \leq 10^{-1} M_{\odot}$, short peak times, and are theorized to be from electron capture collapse to a neutron star or a merger product of ONeMg white dwarf (WD) with another WD, such as AT2018cow.

For every solar mass of formed stars, there are of the order of (3-9) $\cdot 10^{-5}$ mergers between a ONe WD and a CO WD within a Hubble time. For a galaxy like the Milky Way, with a constant star formation history of $4 M_{\odot} yr^{-1}$ for a Hubble time, the current merger rate of CO-ONe WDs is estimated to be (1-4) $\cdot 10^{-4} yr^{-1}$.

Additionally, a ZAMS mass of 15 $M_{\odot}$ that is metal-rich and whose hydrogen envelope is significantly depleted at the time of core-collapse can explain the light curve of AT2022kmm. This model can account for the initial raise and fall profile and the re-brightening of AT2022kmm at $t \sim 18 - 21$ days.

Another alternative model for FBOTs involves the circumstellar interaction of a pulsational pair-instability (PPI) supernova (SN). Specifically, the model focuses on the 41.3 $M_{\odot}$ He star (core of an 80 $M_{\odot}$ star) which has circumstellar matter of mass 0.2 $M_{\odot}$.

A pulsational pair-instability supernova (PPISN) is a type of supernova explosion that occurs when a massive star with a mass of at least 100 times that of the Sun reaches the end of its life. PPISN occurs when the central temperature of the star becomes high enough to ignite pair production, a process where gamma rays are converted into matter-antimatter pairs. This results in a decrease in radiation pressure, causing the core to contract and heat up.

As the core temperature increases, the energy is transferred to the outer layers of the star, causing it to expand and cool. This process repeats itself, resulting in pulsations of the star's surface. However, as the core temperature reaches a critical value, the pair production process becomes so efficient that it causes a runaway thermonuclear explosion, leading to a supernova.

The PPISN explosion is unique in that it is powered by a combination of nuclear burning and radiation pressure, rather than just nuclear burning as in other types of supernovae. The energy released in the explosion is enormous, with up to 10^{53} ergs being released in a matter of seconds. This energy can cause the star to completely disintegrate, leaving behind only a compact remnant such as a black hole or a neutron star.

PPISN explosions are thought to be rare events, occurring only in the most massive stars, and they are important for our understanding of the evolution of the universe and the formation of black holes.

Chapter 2

Materials and Methods

The methods involved in the project are illustrated here.

2.1 Understanding and application of Data Reduction for Astronomical images:

Data reduction is the process of reducing raw data acquired from an astronomical instrument to a form that can be analyzed and interpreted. In astronomical imaging, this process involves several steps to remove instrumental and environmental effects, enhance the signal-to-noise ratio, and extract astrophysical information. The following is an overview of the data reduction process for astronomical images.

The first step is to obtain a raw image from the instrument. This can be in the form of a digital image file, a set of FITS files, or a data cube. The raw image contains information about the light detected by the instrument, including the signal from the astronomical object of interest and the noise introduced by the instrument and the environment.

The next task involves addressing instrumental effects. This involves two main steps: subtracting the bias and performing flat-field correction. Bias subtraction is necessary to eliminate the signal generated by the instrument when there is no light present. This is caused by the offset voltage and ensures that no negative counts occur during the readout. Flat-field correction is performed to account for variations in the instrument's sensitivity across the entire field of view. These variations can be caused by several factors, such as differences in sensitivity among pixels in the detector, the presence of dust on the filter or the glass window covering the detector, and vignetting. To achieve this correction, flats are obtained by uniformly illuminating the CCD. Twilight flats are images of the sky near the zenith taken around sunrise or sunset.

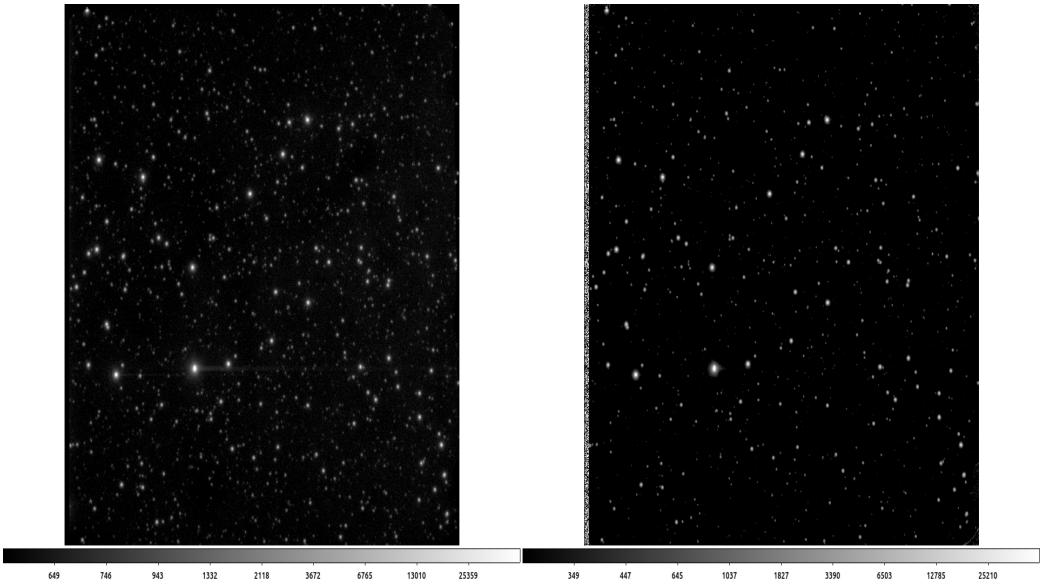

Figure 2.1: Before and after bias subtraction and flat field correction.

Dome flats are images of the inside of the dome (typically of a smooth surface uniformly illuminated, not of the dome itself), illuminated by some light source in the dome. For smaller telescopes an electroluminescent or LED illuminated panel can be used as the light source
correction involves dividing the image by a flat-field image that represents the instrument's response to a uniform light source.

After correcting for instrumental effects, the next step is to align and stack multiple images. This is done to increase the signal-to-noise ratio and remove artifacts such as cosmic rays and hot pixels. The images are aligned using a registration algorithm that accounts for the instrument's pointing and rotation or by finding similar 3-point asterisms (triangles) in images and estimating the affine transformation between them. The stacked image is then created by combining the registered images, typically using a median or average combination method. Cosmic Rays in the images can be removed using the L.A.Cosmic algorithm

The final step is to extract astrophysical information from the reduced image. This involves measuring the brightness and position of astronomical sources, characterizing the morphology of extended sources, and measuring spectral features. The analysis is typically done using specialized software such as IRAF, DS9, or Astropy.

In summary, data reduction for astronomical images is a multi-step process that involves correcting for instrumental effects, aligning and stacking images, and extracting astrophysical information. This process is essential for obtaining accurate and reliable scientific results from astronomical observations.
Necessary tools available in the Astropy project were utilized

2.2 Photometry

UBVRI filters(light of only certain frequency band will be incident on ccd), UBVRI filters are a set of astronomical filters used to observe and study stars, galaxies, and other celestial objects. These filters are named after the wavelength ranges they cover, namely Ultraviolet (U), Blue (B), Visible (V), Red (R), and Infrared (I). The UBVRI system was first introduced by astronomers at the University of Michigan in the 1950s and has since become a standard in the field of astronomy.

The UBVRI filters are designed to capture the light emitted by celestial objects at specific wavelengths, allowing astronomers to analyze the object's spectral properties. Each filter has a specific range of wavelengths that it allows to pass through while blocking other wavelengths of light. The V filter, which covers the visible spectrum, is the most commonly used filter in the UBVRI system.

The U filter, covering the ultraviolet part of the spectrum, has a wavelength range of 320-390 nm. It is particularly useful for studying hot, young stars, as they emit a significant amount of ultraviolet radiation. However, U filters are sensitive to atmospheric effects and require careful calibration.

The B filter, covering the blue part of the spectrum, has a wavelength range of 390-490 nm. It is used to study the temperature and metallicity of stars, as the bluer a star appears, the hotter and more metal-poor it is likely to be. B filters are also sensitive to atmospheric effects but to a lesser degree than U filters.

The V filter, covering the visible part of the spectrum, has a wavelength range of 490-580 nm. It is the most commonly used filter in the UBVRI system and is used to measure the brightness of stars and galaxies. The V filter is less sensitive to atmospheric effects than U and B filters, making it

easier to calibrate.

The R filter, covering the red part of the spectrum, has a wavelength range of 580-700 nm. It is used to study the redshift of galaxies, as the expansion of the universe causes the light emitted by distant galaxies to be shifted towards longer (redder) wavelengths. R filters are also useful for studying the properties of stars, such as their temperature and luminosity.
The I filter, covering the infrared part of the spectrum, has a wavelength range of 700-900 nm. It is used to study the properties of cool stars and to observe objects that emit most of their light in the infrared part of the spectrum, such as molecular clouds and star-forming regions.

In summary, the UBVRI filters are a set of astronomical filters that allow astronomers to observe and study the properties of celestial objects at specific wavelengths. Each filter covers a specific range of wavelengths, allowing astronomers to analyze an object's spectral properties and obtain information about its temperature, metallicity, redshift, and other physical characteristics. While UBVRI filters have some limitations due to atmospheric effects and other factors, they remain an essential tool for astronomers studying the universe.

2.2.1 Aperture Photometry

Identifying the object coordinates and accurate psf, then estimating the magnitude of the object
Aperture photometry is a technique used in astronomy to measure the flux or brightness of a celestial object within a specific aperture or region of the sky. This involves measuring the amount of light that falls within the aperture and subtracting the background noise to obtain the object's flux. The size and shape of the aperture used for photometry depend on the object being studied and the observing conditions.

2.2.2 Airmass correction

Airmass is a measure of the amount of air along the line of sight of the object, light is attenuated by the atmosphere. Accounted for by estimating the airmass from the zenith angle and subtracting the color-scaled airmass from the magnitudes obtained

2.2.3 Standard fields

Standard fields refer to specific visual clusters in the sky that are used as reference points for photometric calibration. These fields are carefully selected to be relatively free of variable or extended sources, and to have a large number of relatively bright and isolated stars that can be used as photometric standards.

The choice of standard fields depends on the wavelength range and instrument used for the observations. For example, the Landolt fields are widely used for optical photometry in the UBVRI filters, while the Two Micron All Sky Survey (2MASS) fields are used for near-infrared photometry.

Standard fields are observed at regular intervals by multiple telescopes and instruments, and the resulting data are used to establish a photometric system and to calibrate the photometric measurements made by other telescopes and instruments. This allows astronomers to compare observations made by different instruments and to perform accurate photometry of astronomical sources.

In addition to photometric calibration, standard fields are also used for astrometric calibration, which involves determining the precise position of astronomical sources on the sky. This is important for studying the motion and distribution of stars and galaxies in the universe.

I did photometry of Standard fields (i.e. PG1633 field) to calibrate the magnitudes for instrumental constant and color correction terms

2.2.4 PSF subtraction photometry

PSF subtraction photometry is a technique used in astronomy to measure the brightness of a celestial object while minimizing the effects of a nearby bright object, such as a star or a galaxy.

The Point Spread Function (PSF) is the pattern of light that a point source (such as a star) creates on an image through a telescope. This pattern is determined by the optics of the telescope and the atmosphere and is typically not perfectly symmetrical.

We create a model of the PSF of the nearby source by fitting a mathematical function to the observed PSF. Next, we subtract the PSF model from the image, which effectively removes the light from the nearby source, leaving only the light from the target object. Finally, they measure the brightness of the target object using standard photometric techniques on the subtracted image.

2.2.5 Template subtraction photometry

Template subtraction photometry is a technique used in astronomy to measure the flux, or brightness, of a source of interest in an astronomical image. The idea behind template subtraction photometry is to subtract a template image, which represents the background and other sources of light in the image, from the image containing the source of interest. The resulting residual image will ideally contain only the flux from the source of interest.
The resulting residual image is then analyzed to measure the flux of the source of interest, using techniques such as aperture photometry or PSF-fitting photometry.

Template subtraction photometry is particularly useful for measuring the flux of faint sources in crowded fields, where other sources of light can interfere with the measurement. It is also useful for studying transient or variable sources, as the template image can be updated to account for changes in the background or other sources of light over time.

Data from the following archives have been used here: ATLAS (Asteroid Terrestrial-impact Last Alert System) the transient survey, ZTF (Zwicky Transient Factory) Bright Transient Survey database and the NASA/IPAC Extragalactic Database. The ATLAS Transient survey provided the forced photometry of AT2022kmm. ZTF and ATLAS are two astronomical survey programs that employ wide-field imaging technology to detect and study a wide range of astrophysical objects in the sky. Both programs use telescopes equipped with advanced digital cameras that capture images of large portions of the sky, allowing them to detect and monitor objects that vary in brightness over time, such as supernovae, asteroids, and comets.

2.2.6 ZTF

ZTF is a collaborative project between several institutions, including the California Institute of Technology, the University of Maryland, and the National Optical Astronomy Observatory. The ZTF telescope is located at the Palomar Observatory in California and uses a 47-square-degree field of view to survey the sky. The program aims to detect and study a wide range of astronomical phenomena, including transient events such as supernovae, novae, and variable stars, as well as moving objects such as asteroids and comets. ZTF's imaging capabilities are also used for follow-up observations of other astronomical events, such as gravitational waves and gamma-ray bursts.

2.2.7 ATLAS

ATLAS, on the other hand, is a project that focuses specifically on detecting and tracking asteroids that could potentially impact the Earth. The program operates two telescopes, one located in Hawaii and the other in Chile, both with a field of view of approximately 100 square degrees. ATLAS uses a technique called "differential imaging," which involves taking multiple images of the same region of the sky and subtracting them from one another to identify objects that have changed in brightness. This method is particularly useful for detecting faint objects that may be missed by other surveys. In addition to detecting potentially hazardous asteroids, ATLAS also studies other transient phenomena such as supernovae and variable stars.
Both ZTF and ATLAS are important astronomical surveys that contribute significantly to our understanding of the universe. Their wide-field imaging capabilities and advanced digital cameras allow them to detect and study a wide range of astrophysical objects, from distant supernovae to potentially hazardous asteroids. These surveys are also important for monitoring the sky and identifying objects that could pose a threat to Earth, as well as for follow-up observations of other astronomical events. As such, they play a crucial role in advancing our knowledge of the cosmos and helping to ensure the safety of our planet.

The ATLAS Forced Photometry Tool is a software package that allows astronomers to measure the brightness and position of objects in astronomical images, even when those objects are not easily visible by eye. This is achieved by using a technique called forced photometry, which involves measuring the brightness of a known location in an image and subtracting out the light from other objects in the vicinity.

The ATLAS Forced Photometry Tool is particularly useful for studying objects that are faint or hard to detect, such as asteroids, comets, and variable stars. It can be used to extract photometric measurements from a wide range of astronomical images, including single-band and multi-band images, as well as images taken at different times or with different telescopes.

One of the key advantages of the ATLAS Forced Photometry Tool is its reliability. The software has been extensively tested and validated on a wide range of astronomical data sets, and it has been shown to produce accurate and reliable photometric measurements even in challenging conditions. This makes it a valuable tool for astronomers studying a wide range of astrophysical objects and phenomena.

The output of the ATLAS Forced Photometry Tool is a table of photometric measurements for each object in the image. This table includes the

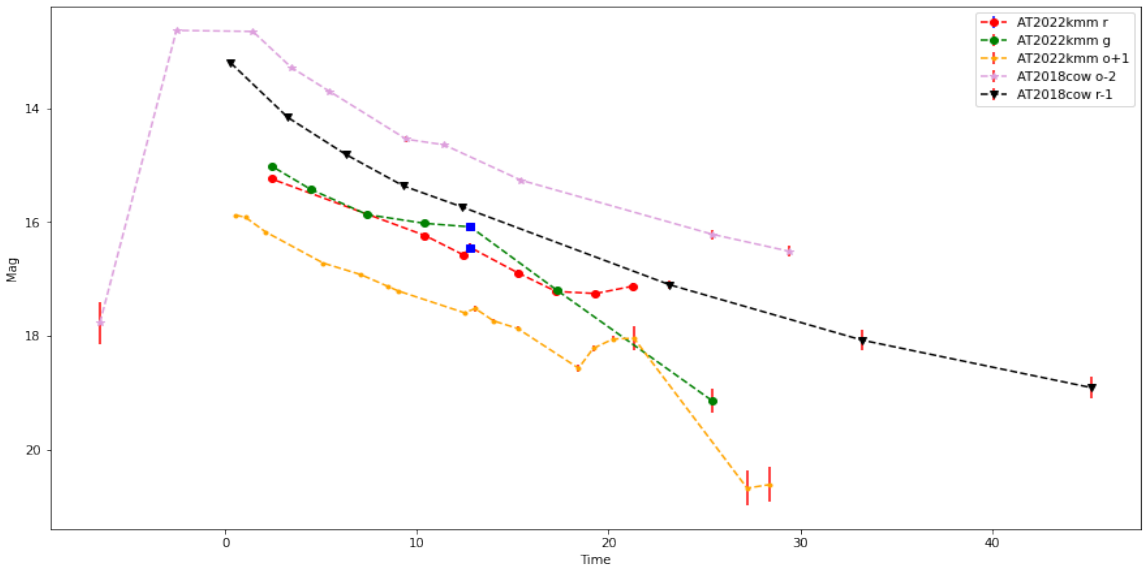

Figure 2.2: AT2022kmm (ZTF22aalfjze) and AT2018cow (ZTF18abcfcoo). The o band data is from forced photometry of ATLAS transient survey data of AT2022kmm and AT2018cow. The r and g band data are from the ZTF survey

measured brightness of each object in each band, as well as estimates of the object's position and size. The tool also provides a number of diagnostic plots and statistics to help users evaluate the quality of their photometric measurements and identify potential sources of error.

Overall, the ATLAS Forced Photometry Tool is a powerful and reliable software package that allows astronomers to extract accurate photometric measurements from a wide range of astronomical images. Its ability to detect and measure faint or hard-to-detect objects makes it a valuable tool for studying a wide range of astrophysical phenomena, and its reliability and ease of use make it a popular choice among researchers in the field.

light curves of AT2022kmm and AT2018cow from these surveys are shown in Fig. 2.2. Forced photometry was used here.
orange-ATLAS data from ATLAS forced photometry AT2022kmm and AT2018cow
r band data from ZTF data of Object ZTF18abcfcoo AT2018cow
r and g band data from ZTF data of Object ZTF22aalfjze AT2022kmm

2.3 Spectroscopic Data Reduction:

Spectroscopy is a powerful tool in astronomy that allows us to study the physical properties of astronomical objects such as stars, galaxies, and interstellar matter. Spectroscopic data reduction is the process of transforming raw data acquired by a spectrograph into a form that can be analyzed and interpreted. This process involves several steps to remove instrumental effects, correct for atmospheric and calibration issues, and extract astrophysical information from the spectra.

The first step in spectroscopic data reduction is to obtain the raw data from the spectrograph. The raw data is typically in the form of a 2D image or a series of 1D spectra, depending on the spectrograph's configuration. The raw data contains information about the light detected by the spectrograph, including the spectral intensity and wavelength.

The second step is to remove instrumental effects such as dark current, bias, and pixel-to-pixel variations in sensitivity. The removal of these instrumental effects is essential to obtain a clean spectrum.
The next step is to extract the spectrum from the 2D image or series of 1D spectra. This involves tracing the spectral orders and extracting the spectra from the background. Tracing the spectral orders is the process of determining the position of the spectral features in the 2D image or 1D spectra.

Figure 2.4: (l) The raw spectrum of Feige 67 is shown again, with (r) the background extraction region marked as a shaded region on either side of the spectral trace.

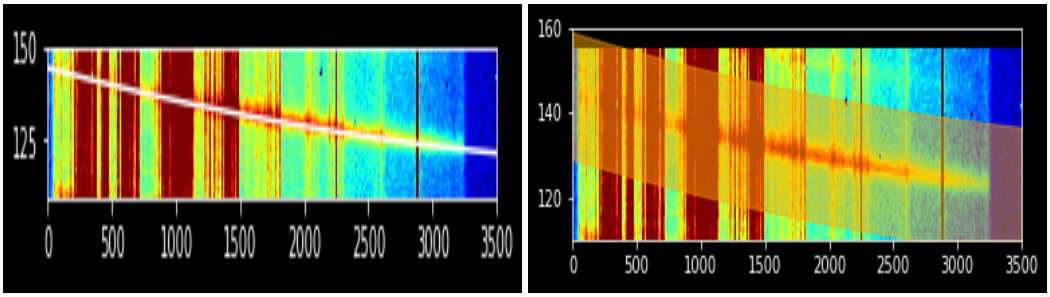

The extraction of the spectrum from the background involves subtracting the background signal from the spectrum. The background signal can come from sources such as the sky, the instrument, or the detector itself.
The extracted spectrum is then wavelength calibrated, which involves deter-

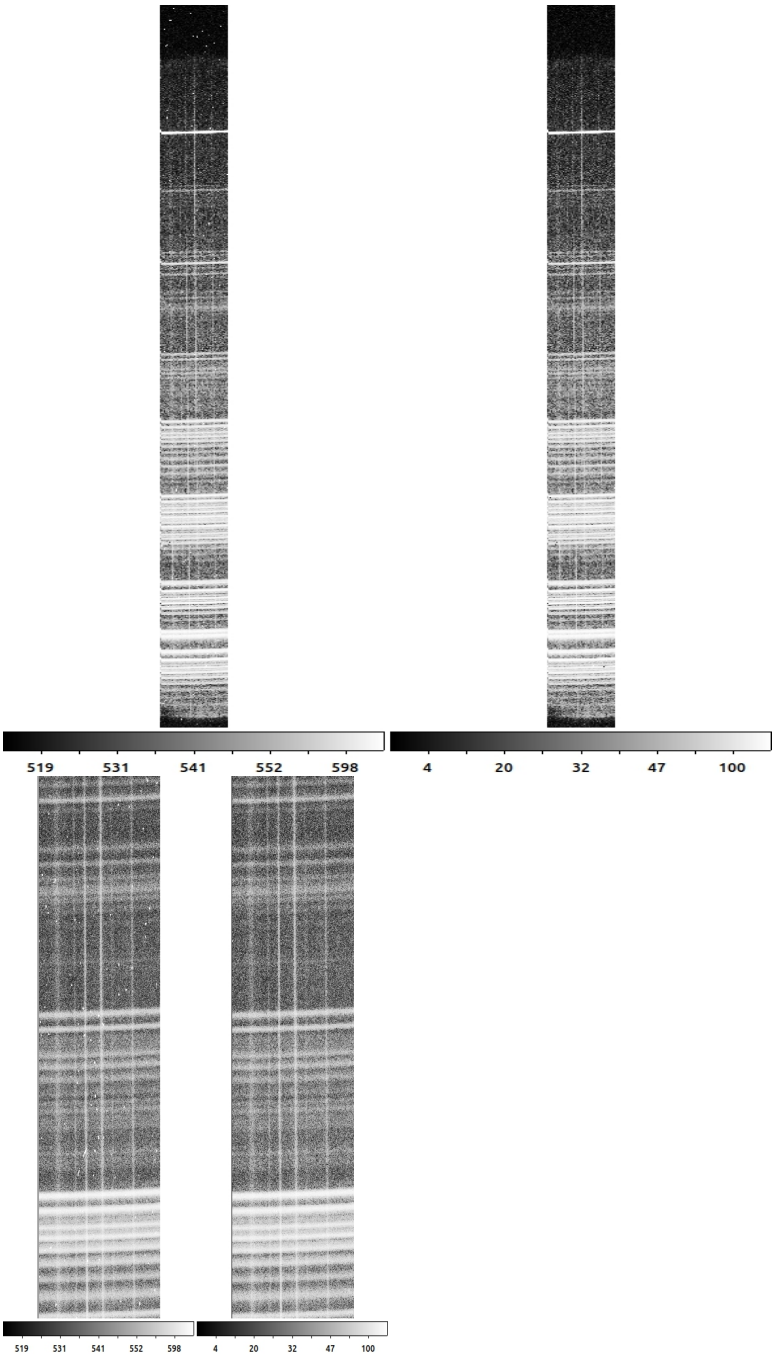

Figure 2.3: (l) Shows the difference of the raw image the bias subtracted, cosmic ray removed spectra on the CCD. (r) A region is magnified

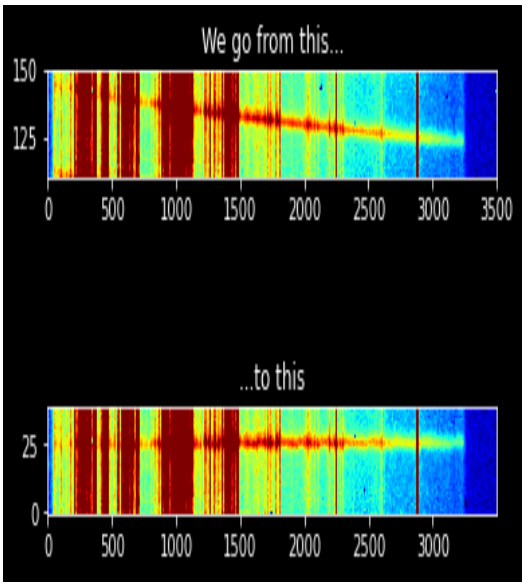

Figure 2.5: The figure shows CCD images of the raw spectrum of the spectrophotometric calibration star Feige 67, and its background corrected, traced, spectrum.

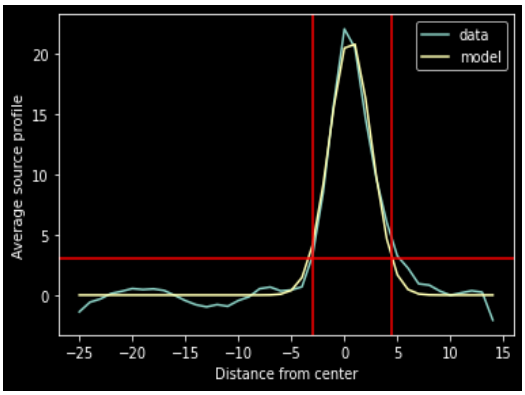

Figure 2.6: Background removal and modelling

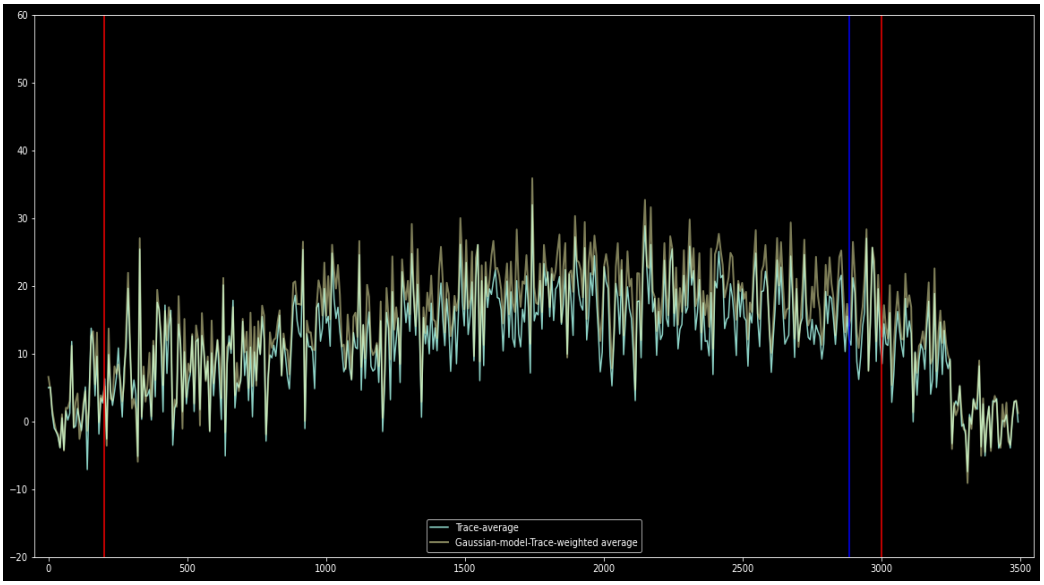

Figure 2.7: Raw spectrum before wavelength calibration

mining the relationship between the pixel position in the spectrograph and the corresponding wavelength of the light. This calibration is typically done using a set of calibration spectra, such as a calibration lamp or a reference star. The calibration spectra provide a set of known spectral features that can be used to determine the pixel-to-wavelength calibration of the spectrograph.

The next step is to correct atmospheric effects, such as telluric absorption and atmospheric emission lines. The Earth's atmosphere absorbs and emits light at specific wavelengths, which can obscure the astrophysical features in

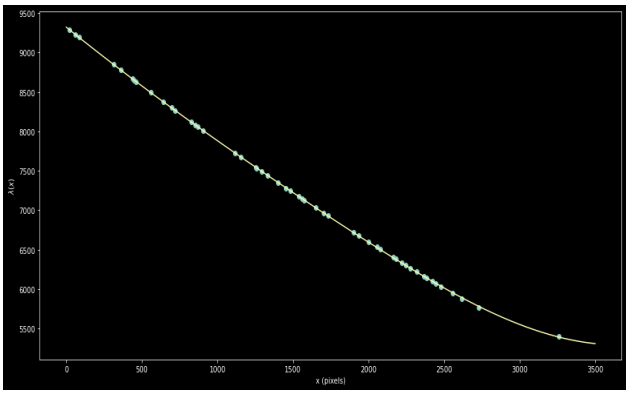

Figure 2.8: Wavelength calibration

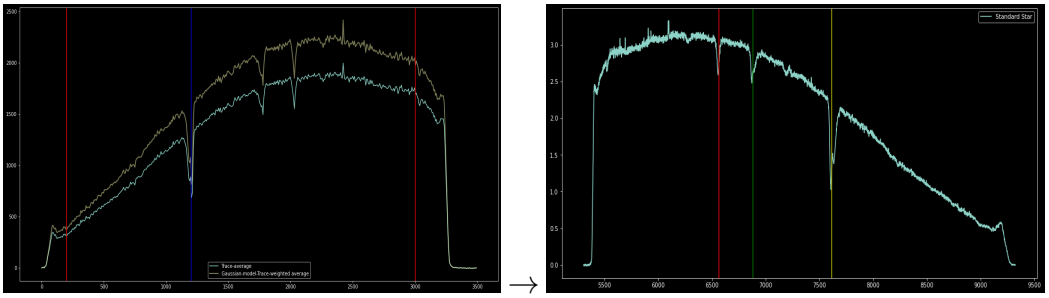

Figure 2.9: Calibrated sectrum

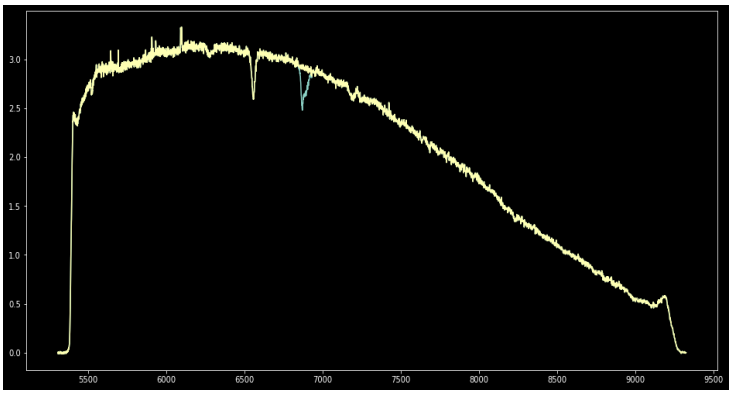

Figure 2.10: Telluric line removal

the spectrum. The correction for atmospheric effects is typically done using a dedicated software package that models the Earth's atmosphere and removes the telluric absorption and emission features from the spectrum.

Once the spectrum has been corrected for instrumental and atmospheric effects, the next step is to flux calibrate the spectrum. Flux calibration is the process of determining the absolute flux of the spectrum in physical units such as ergs/s/cm2/Å. This calibration is typically done using a standard star with a known flux calibration. The standard star is observed under photometric conditions and provides a reference spectrum with a known flux calibration. The observed spectrum is then compared to the reference spectrum to determine the flux calibration of the spectrograph.

Spectroscopic data reduction of Feige67 is illustrated

Finally, the spectrum is analyzed to extract astrophysical information such as the chemical composition, temperature, and velocity of the source. This analysis is typically done using specialized software packages that model the astrophysical processes that produce the spectral features. For example, the chemical composition of a star can be determined by comparing the observed

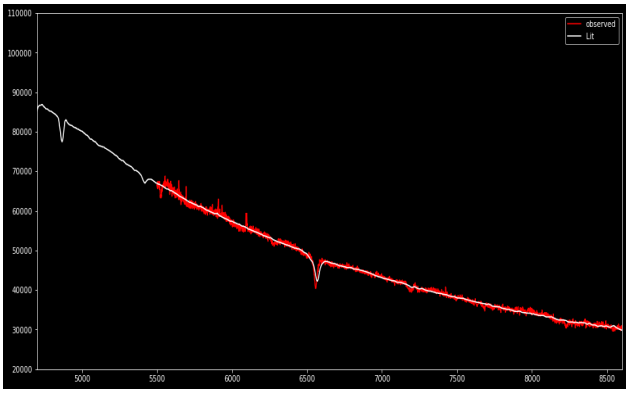

Figure 2.11: Observed spectrum after flux calibration against standard spectrum

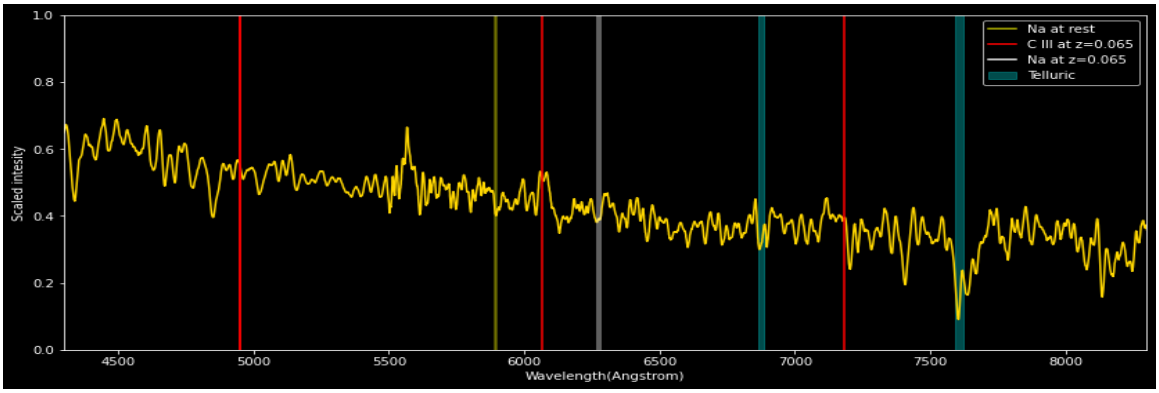

Figure 2.12: Final spectrum with boxcar smoothing with width=9

spectrum to a model spectrum that includes the expected spectral features of the elements present in the star.

Spectrum from AT2022kmm study
From the spectrum of AT2022kmm the redshift of the host galaxy was accurately estimated and the absence of Hydrogen was suspected

The Sodium "D-lines" are commonly used in astronomy to estimate the redshift of celestial objects such as galaxies, quasars, and other extra-galactic sources. The reason for this is twofold:
(1) NaI has strong resonance lines at 589.0 nm and 589.6 nm, and,
(2) The Na has a small, but significant, abundance in the ISM of most galaxies, including the Milky Way, and the host the galaxy of the supernova.

When light from a distant celestial object travels through space, it can be affected by the motion of the object and the space it travels through. If the object is moving away from us, the wavelength of the light it emits will be shifted towards longer wavelengths (redshifted). By comparing the observed wavelength of the sodium D-lines in the spectrum of a celestial object to their known rest wavelength, astronomers can determine the object's redshift.

In summary, spectroscopic data reduction is a multi-step process that involves correcting for instrumental and atmospheric effects, extracting the spectrum, calibrating the wavelength and flux, and analyzing the spectrum to extract astrophysical information

Brief description of numerical codes used in this work

To generate light curves we first need to model the state just prior the explosion. We also require a numerical code that solves self-consistent radiation transport in an expanding ejecta to model the light curve. We also use codes to compare the spectrum with templates from archivial observations

2.4 MESA

MESA (Modules for Experiments in Stellar Astrophysics) is a software package designed for modeling the evolution and internal structure of stars. It is used by astrophysicists to study a wide range of phenomena, from the formation of stars and planets to the explosive deaths of massive stars as supernovae.

MESA is a modular code, which means that it consists of a collection of interchangeable modules that can be combined to create a customized model of a star. These modules include modules for the equation of state, nuclear reactions, convection, and stellar evolution, among others. MESA also includes a user-friendly interface and visualization tools that allow researchers to easily create and analyze stellar models.

One of the key features of MESA is its ability to model a wide range of stellar masses and compositions, from low-mass red dwarfs to massive blue supergiants. It can also simulate the effects of various physical processes, such as rotation, magnetic fields, and binary interactions, on the evolution

of stars.

MESA is particularly useful for studying the evolution of stars beyond the main sequence, where complex interactions between convection, nuclear reactions, and other physical processes can lead to a wide range of outcomes. For example, MESA has been used to study the formation of white dwarfs, neutron stars, and black holes, as well as the properties of red giants, asymptotic giant branch stars, and other evolved stars.

MESA is an open-source code, which means that it is freely available to researchers and can be modified and improved by the community. This has led to the development of a large and active user community that contributes to the ongoing development and improvement of the code.

Overall, MESA is a powerful tool for studying the evolution and internal structure of stars and has been used to make important contributions to our understanding of stellar astrophysics.

2.5 SNEC

SuperNova Explosion Code (SNEC) is an open-source, Lagrangian code used to model the hydrodynamics and equilibrium-diffusion radiation transport in the expanding envelopes of core-collapse supernovae (CCSNe). This code takes into account the effects of recombination and the presence of radioactive nickel and can generate bolometric and multi-color light curves for different observed wavelengths using the blackbody approximation.
To create a model of a progenitor star's envelope and its explosion energy, SNEC utilizes a spherically-symmetric Lagrangian radiation-hydrodynamics approach. However, the composition profile of the star as generated by the MESA (Modules for Experiments in Stellar Astrophysics) software may contain abrupt variations due to convective dragging. To account for this, a boxcar smoothing method can be applied to achieve a smoother profile.
During a core-collapse supernova, radioactive 56Ni is generated in the inner regions of the star and then mixed outward by hydrodynamic instabilities. The gamma rays emitted during the decay of 56Ni to 56Co and 56Fe provide an additional source of energy in the explosion. While the current version of SNEC does not include a nuclear reaction network, the user can manually specify the amount and distribution of 56Ni to study its impact on light curves.

It is important to note that nucleosynthetic yields can be affected by various factors, including the launch of the explosion, its location in the star's mass and spatial coordinates, and uncertainties in the structure and composition of the layers where explosive burning occurs. By manually specifying the 56Ni yield, these uncertainties can be removed from the models, and the user has complete control over the radioactive heating, making it useful for studying the impact on light curves in detail.

2.6 SNID

The Stephane Blondin Supernova Identification (*SNID*) code is a computer program used for identifying the type and parameters of supernovae from their observed spectra. It was developed by Stéphane Blondin in 2005 and has since become widely used in the astronomical community.
SNID works by comparing the observed spectrum of a supernova to a large library of template spectra of known supernova types. It uses a χ^2 minimization technique to determine the best-fit supernova type and estimate the supernova's redshift, age, and velocity.
The program can also be used to estimate interstellar reddening, which is the absorption of light by dust in the interstellar medium. SNID is particularly useful for identifying supernovae that are not well-matched by existing templates, as it allows users to create their own templates by combining existing ones.
Overall, the SNID code has been instrumental in advancing our understanding of supernovae and has been used in many groundbreaking studies of these fascinating astronomical events.

2.7 AstroDASH

AstroDASH is a deep-learning model developed for the automated spectral classification of supernovae. It was developed by a team of astronomers at the University of California, Berkeley in 2018.
The model is trained on a large dataset of supernova spectra, with the goal of accurately classifying them into various types based on their observed features. AstroDASH uses a convolutional neural network (CNN) architecture, which is designed to recognize patterns in spectral data and make predictions based on those patterns.
One of the key advantages of AstroDASH is its ability to quickly and accurately classify large numbers of supernova spectra. This is particularly

important for large-scale surveys that produce vast amounts of data, as it allows astronomers to efficiently identify and study large numbers of supernovae.

Comparing AstroDASH and SNID

DASH relies on a pre-existing template library, which may not include all possible spectral types whereas SNID allows for the creation of custom templates, which can be useful for studying rare or unusual supernova types, DASH can classify a large number of spectra at once, making it useful for large surveys and SNID is not as fast for large surveys

Chapter 3

Results and Discussion

AT 2022kmm was discovered on UT 2022 May 23.5211 by the ATLAS-MLO-ATLAS-01, with the internal survey name ATLAS22okh, and reported on the Transient Name Server (TNS) on UT 2022 May 24.0122 (J. Tonry), with a discovery magnitude of orange-ATLAS = 14.696±0.011 mag. Forced photometry on images taken by ZTF internal name ZTF22aalfjze on UT 2022 May 25.44 and 25.419 in g and r at 15.017 and 15.239 mags, respectively(with non-detections in ZTF g, r, and orange-ATLAS down to 19.56, 20.46 and 18.43 mags, respectively). Our final non-detection in orange-ATLAS was on UT 2022 June 19.272 at $\geq 19.95 \pm 0.460$ mags.

Photometric data from HCT observation on 2022-06-04
Bes I 16.572+/-0.032
Bes R 16.442+/-0.041
Bes V 16.275+/-0.048
Bes B 15.750+/-0.068
Bes U 16.010+/-0.057
$(g - r) \approx -0.363 \pm 0.087$[1]

Non-detection from HCT (observation date: 2022-10-22)
3 Bes I 20.161+/-0.067 4 Bes R 21.710+/-0.228

Photometric data of AT2018cow from HCT observation on 2018-07-06

object	V	B-V	U-B	V-R	V-I
AT2018cow	16.841±0.048	0.323 ± 0.083	-0.929 ± 0.089	0.115 ± 0.063	0.299±0.0573

Bes I 16.542+/-0.0324
Bes R 16.725+/-0.0415
Bes V 16.841+/-0.0486
Bes B 16.518+/-0.0687

[1]Filter Transformations:
g = V+0.60*(B-V) - 0.12
r = V-0.42*(B-V) + 0.11

Bes U 15.588+/-0.057
$(g - r) \approx -0.559 \pm 0.085$
We conducted a study to investigate the impact of significant mass loss during the evolution of massive stars on their presupernova structure and resulting supernova (SN) light curve. We assumed that the mass loss occurred rapidly, but not so fast that the star could not adjust to a new equilibrium. Instead of simulating uncertain mass loss mechanisms, we conducted a controlled experiment by systematically removing material from the envelope of a 15 $M_{\odot}$ ZAMS star at the start of Helium burning. This study is similar to a previous one by Morozova et al, which also explored the effects of mass loss on Type II SN light curves.

Our focus was to explain the AT2022kmm's light curve, the initial raise and fall profile, and the re-brightening of AT 2022kmm at t$\sim 18 - 21$ days. From the light curve and spectrum observed on 04-06-22, we were able to rule out the event being a Type 1a SN due to the absence of Si II line and the short rise and fall times were distinct from the characteristic light curve of type 1a.
In Figure 3.1 it's compared against a architypical type 1a SN 2011fe and a

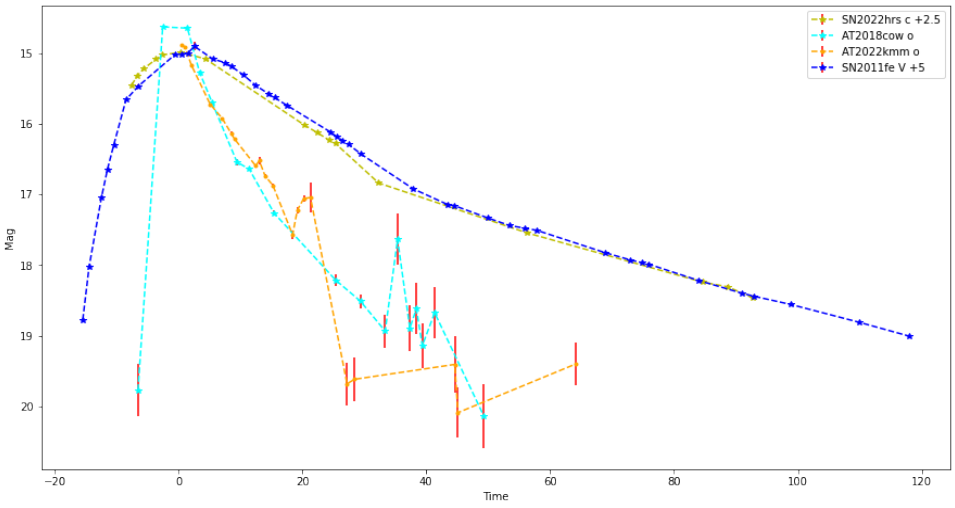

Figure 3.1: FBOTs compared to SN 2011fe a architypical type 1a and SN 2022hrs a recently observed type 1a SN

recently observed type 1a SN 2022hrs
There are few discernible features from the spectrum due to the early-time photosphere being hot. Spectrum was neither classified identified by Stéphane Blondin's Supernova Identification[SNID] code nor by AstroDASH

Compared against prototypical type 1c SN 1994I. But spectra and light

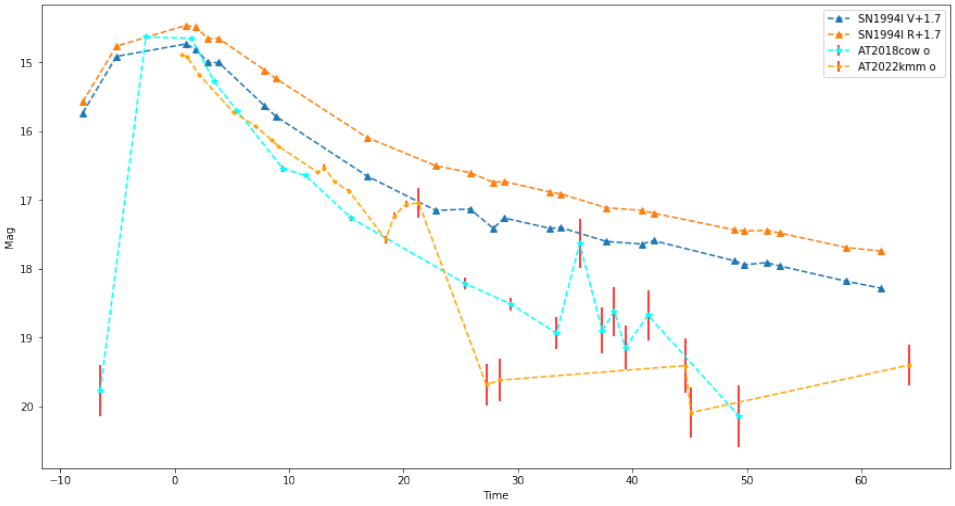

Figure 3.2: FBOTs compared against architypical type 1c SN 1994I

curve didn't conform to type 1c
Redshift was estimated by finding the sodium D-lines of the host galaxy and

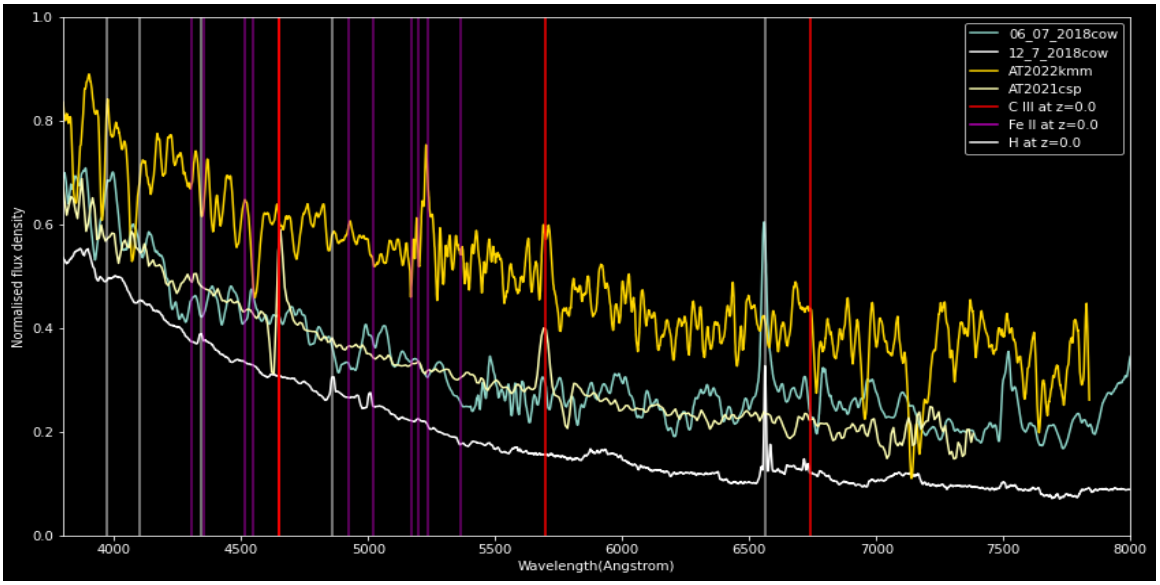

Figure 3.3: Spectra of FBOTs. Spectra of AT2018cow taken 20 and 26 days after peak, the H-α line is attributed to the host galaxy

comparing it with the same of our galaxy. We get Redhift=0.065 implying distance=296.7 Mpc (H_0 set as $67.5 km/s/Mpc$).

From observed spectrum's C III line the ejecta velocity $V_{ej} \sim 3700 - 4500$ km s^{-1}. This is estimate from the Doppler spread of the C III 5696 Å line. There is a reading by both ZTF and the ATLAS survey in 2 bands each for the 2nd day after peak.

Filter name	ZTF g	ATLAS c	ZTF r	ATLAS o
λ_{eff} Å	4722.1	5182.42	6338.62	6629.82
Flux μJy	3574.374	3340	2913.3992	3097.5

Table 3.1: Table shows central flux at the centriod of each filter.

temperature can be calculated using these readings by fitting a blackbody curve

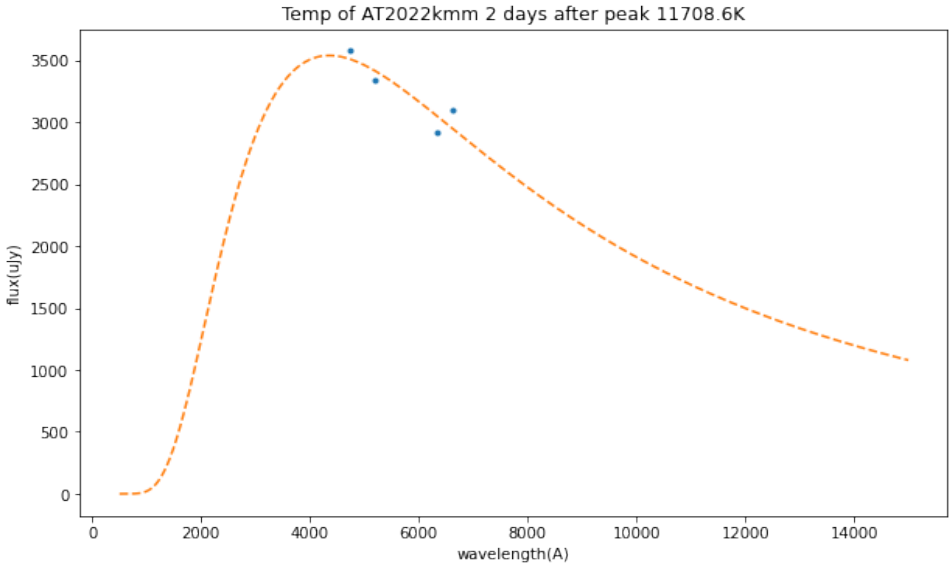

Figure 3.4: Estimating temperature of AT 2022kmm

Re-brightening of AT 2022kmm at t$\sim 18 - 21$ days could be the ejecta interacting with the binary companion or dense medium at $41 - 50$ AU.
On the other hand this could have been caused by metal ions capturing electrons. For hydrogen or helium medium to recombine and cause a such brightening lot of material is required $\sim 10 M_{\odot}$, but similar energy can be released by Iron group ions or by ions of oxygen group with a much lower amount of material. Rapidly thinning ejecta that's metal-rich satisfies the energetics of the re-brightening phase.

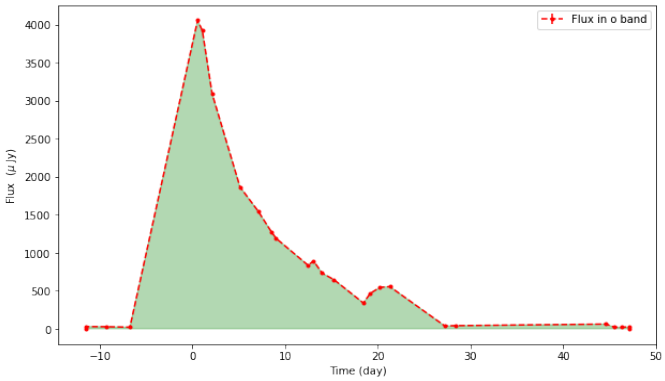

Figure 3.5: Shaded area shows the total bolometric luminosity Atlas.orange $\lambda_{eff} = 6629.82$Å and Wavelength range: $5582.07 - 8249.18$Å Total energy in Atlas orange band(55 days) $6.5 - 7.2 \times 10^{49}$ erg

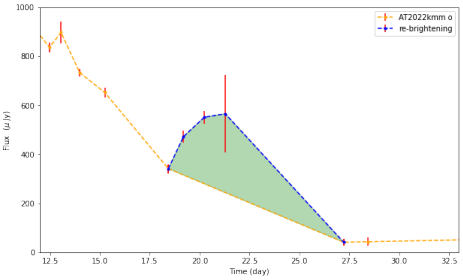

Figure 3.6: The shaded area is used to estimate the energy released during the rebrightening

We estimated the total energy in o-band above the continuam during this phase $2.29 - 2.43 \times 10^{48}$erg Figure 3.6
We utilized the MESA release version release r22.11.1 and assumed a solar metallicity of Z=0.02. Convection was determined using the Ledoux criterion, and we employed MESA's standard settings in Test_suite 12_$M_\odot$ _pre_ms_to_core_collapse but changing the ZAMS mass to 15 $M_\odot$ and introduced mass loss at the start of Helium burning. The precise point of stripping has little influence on the resulting light curve.(Morozova et al., 2015)
When using SNEC, a detailed understanding of the core structure is not necessary as the light curve is primarily determined by the outer regions and the hydrogen-rich envelope. Additionally, we manually initiate explosions and introduce ^{56}Ni to the simulation.

Simulation with ZAMS mass 15 $M_\odot$:

The module `12M_pre_ms_to_core_collapse` from the MESA Test_suite was modified. In parameter set `inlist_mass_Z_wind_rotation`, `initial_mass` was set to 15 and `initial_z` set to 0.02, synthetic mass loss was introduced via "wind controls" in parameter set `inlist_to_end _core_c_burn` by setting a negative `mass_change`. The extent of mass loss was controlled by `min_star_mass_for_loss`, for better fine tuning of the final mass in parameter set `inlist_to_lgTmax` wind controls were again introduced and mass_change was set to a negative value and `wind_H_envelope_limit` invoked, Winds automatically shut off when star_mass - he_core_mass mass is less than this limit. All masses are in Msun($M_\odot$) units.
The MESA simulation stops when `fe_core_infall_` limit crosses 10^7cm/s i.e. stop if atleast `fe_core_infall_mass` of material has speed greater than this, at a location interior to `fe_core_mass`, in cm/s
SNEC is a computational tool that is designed to simulate both thermal bomb and piston-driven explosions. In the case of a piston-driven explosion, the first two computational cells of the explosion profile are propelled outward by a piston with a velocity of `piston vel`, measured in centimeters per second. This occurs during a specific time interval that is defined by the parameters piston `tstart` and piston `tend`, both measured in units of seconds and specified in the parameters file.
However, in the piston-driven case, it is not easy to accurately calculate the total energy that is transferred to the exploding star beforehand. This is due to the complex nature of the explosion and the multiple factors that can

affect the energy transfer.
Explosion parameters are set as follows: Explosion type ="Thermal_Bomb" as an estimate of the energy in Atlas orange band is known to be $\sim 10^{49}$erg and temperature is estimated $\sim$ 11kK, implying an energetic explosion, and by calculating the gravitational binding energies of the simulated star at core-collapse(`fe_core_infall_limit`) and when the core reaches nuclear density $\sim 10^{14}$g/cc
Grav E at core-collapse(`fe_core_infall_limit`) $\sim 5 \times 10^{51}$ erg
Grav E when the core reaches nuclear density $\sim 1.6 \times 10^{53}$ erg
Even if 99% energy is carried out by neutrinoes, the 1 percent energy $\sim 1.6 \times 10^{51}$ erg deposited into the ejecta should power the light curve
Total energy =1e51 erg, 0.1 $M_\odot$ is the amount of ^{56}Ni generated this is controlled by `Ni_mass` value, `Ni_boundary_mass` is 3 solar mass i.e. ^{56}Ni is deposited outside of the $1.4M_\odot$ core and in the interior of $3M_\odot$
Multile SNEC simulations were performed by varying the above parameters
Boxcar smoothing with a kernel of $0.4M_\odot$ is switched on

No.	Mass at Core-collapse ($M_\odot$)	Amount of ^{56}Ni ($M_\odot$)	Hydrogen envelop ($M_\odot$)	Explosion Energy (erg)	Figure
1	> 6	0.1	> 1.5	10^{51}	Figure 3.6
2	5.6	0.1	0.9	10^{51}	Figure 3.7
3	5.6	0.1	0.9	2×10^{51}	Figure 3.8
4	5.6	0.05	0.9	10^{51}	Figure 3.9
5	5.4	0.1	0.7	10^{51}	Figure 3.10
6	5.4	0.05	0.7	10^{51}	Figure 3.11
7	5.2	0.1	0.5	10^{51}	Figure 3.12
8	5.2	0.05	0.5	10^{51}	Figure 3.13
9	5.1	0.1	0.4	10^{51}	Figure 3.14
10	5.1	0.05	0.4	10^{51}	Figure 3.15
11	5.1	0.01	0.4	10^{51}	Figure 3.16
12	5.1	0.02-0.03	0.4	10^{51}	Figure 3.17
13	5	0.05-0.1	0.3	$1 - 2 \times 10^{51}$	Figure 3.18
14	4.6	0.1	0.3	10^{51}	Figure 3.19
15	4.5	0.1	0.3	10^{51}	Figure 3.20
16	4.3	0.1	0.3	10^{51}	Figure 3.21
17	4.1	0.1	0.3	10^{51}	Figure 3.22
18	3.7	0.1	0.3	10^{51}	Figure 3.23

Table 3.2: Explosion parameters of stars of ZAMS mass of $15M_\odot$ with extreme mass loss.

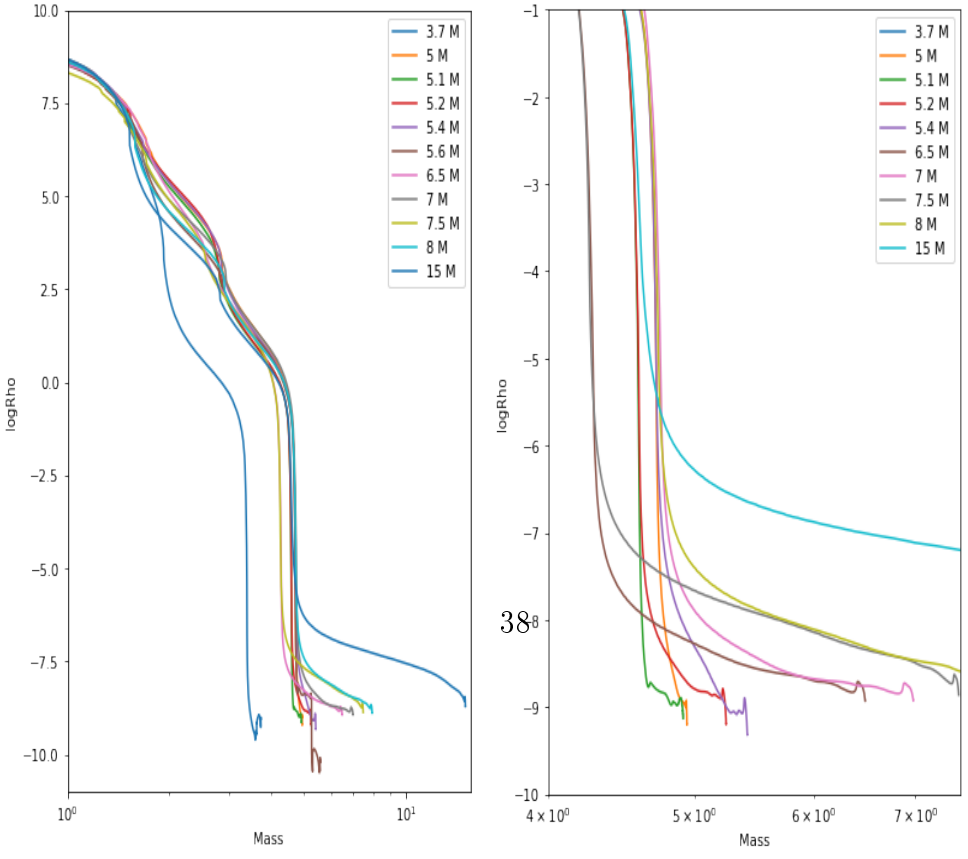

1) MESA simulations with `min_star_mass_for_loss` set to 6.5, 7, 7.5, 8 Solar mass were compiled and the output profile is loaded to SNEC and exploded with the above mentioned parameters

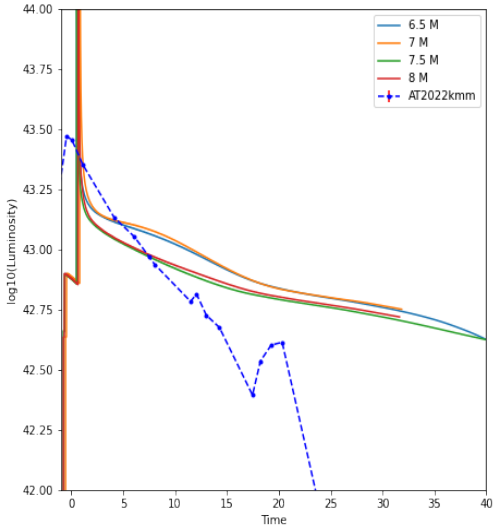

Figure 3.8: Figure shows SNEC outputs for progenitor with 15 $M_{\odot}$ ZAMS mass and mass loss leading to 6.5,7,7.5,8 $M_{\odot}$ prior to core-collapse.

The luminosity doesn't fall rapidly due to the large amount of Hydrogen. The hydrogen recombination powers the light curve for an extended period of time leading to the

2) In the case of 5.6 $M_{\odot}$ pre-explosion progenitor star, hydrogen envelope is reduced to 0.9 $M_{\odot}$ by setting `min_star _mass_for_loss` to 5.6 $M_{\odot}$ in MESA and the output profile is loaded to SNEC and exploded with the above mentioned parameters.

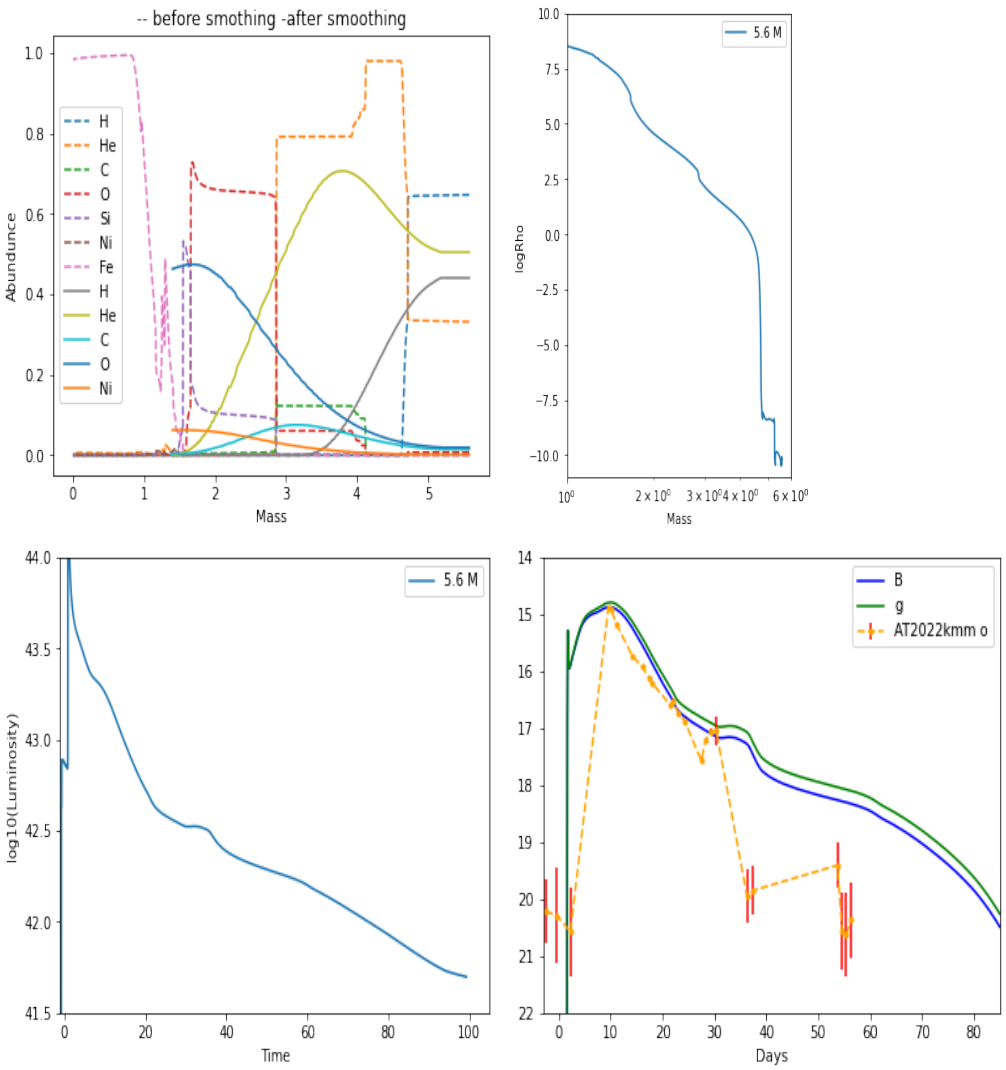

Figure 3.9: Figure shows MESA and SNEC outputs for progenitor with 15 $M_{\odot}$ ZAMS mass and mass loss leading to 5.6 $M_{\odot}$ prior to core-collapse. Top left pre-explosion composition profile from MESA. Top right density profile. Bottom left SNEC bolometric lightcurve. Bottom right Magnitudes in Bes B and SDSS g

The light curve for the first 25 days agrees well with the observed light curve, initial rise, fall of luminosity for 10-15 days and re-brightening phase at the required epoch was approximately generated, but it fails to get the rapid fall in luminosity of the next phase.
3) Repeating the 5.6 $M_{\odot}$ star explosion with twice the explosion energy, i.e. total energy $=2\times10^{51}$ erg.

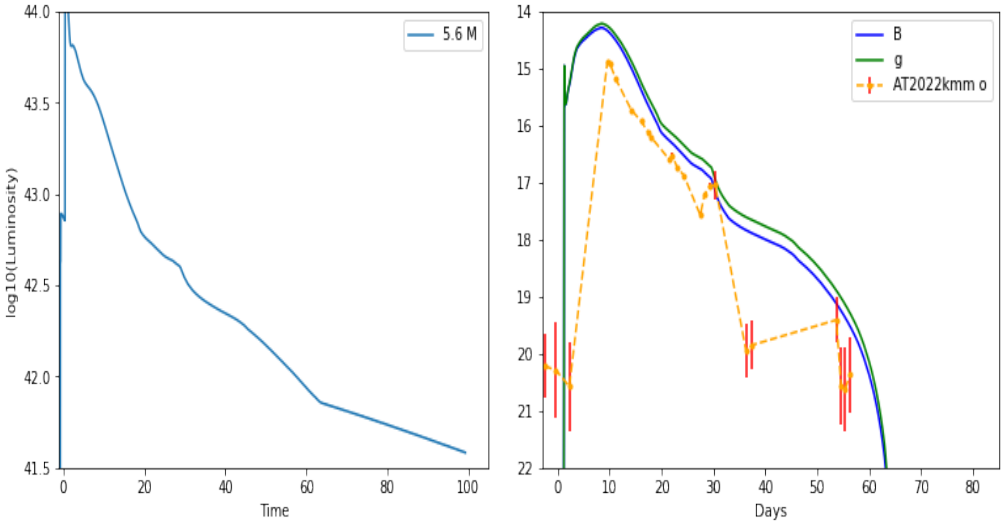

Figure 3.10: Figure shows SNEC outputs for progenitor with 15 $M_{\odot}$ ZAMS mass and mass loss leading to 5.6 $M_{\odot}$ prior to core-collapse exploded with twice the explosion energy. Left SNEC bolometric lightcurve. Right Magnitudes in Bes B and SDSS g

This had the expected consequences: the peak brightness incresed and the re-brightening happened earlier as the higher energy evolves the ejecta faster.
4) Reducing the amount of ^{56}Ni generated in the same progenitor to 0.05 M

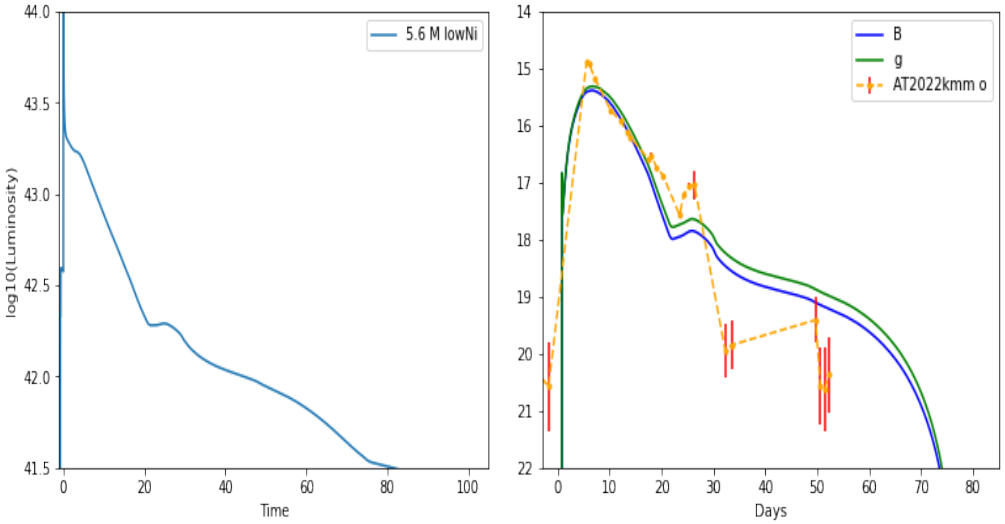

Figure 3.11: Figure shows SNEC outputs for progenitor with 15 $M_{\odot}$ ZAMS mass and mass loss leading to 5.6 $M_{\odot}$ prior to core-collapse exploded with half the amount of ^{56}Ni. (Left) SNEC bolometric lightcurve. (Right) Magnitudes in Bes B and SDSS g

Lowering the `Ni_mass` showed the significance of the radioactive decay of ^{56}Ni that continous to power the lightcurve after the end of recombination of elements in the envelope. The lower `Ni_mass` was expected to generated the post re-brightening rapid fall in brightness but failed.
5) In the case of 5.4 $M_{\odot}$ pre-explosion progenitor star,the star was evolved similar to 5.6 $M_{\odot}$ star and `wind_H_envelope _limit` was set to 0.7 $M_{\odot}$ that limited the hydrogen envelope to 0.7 $M_{\odot}$

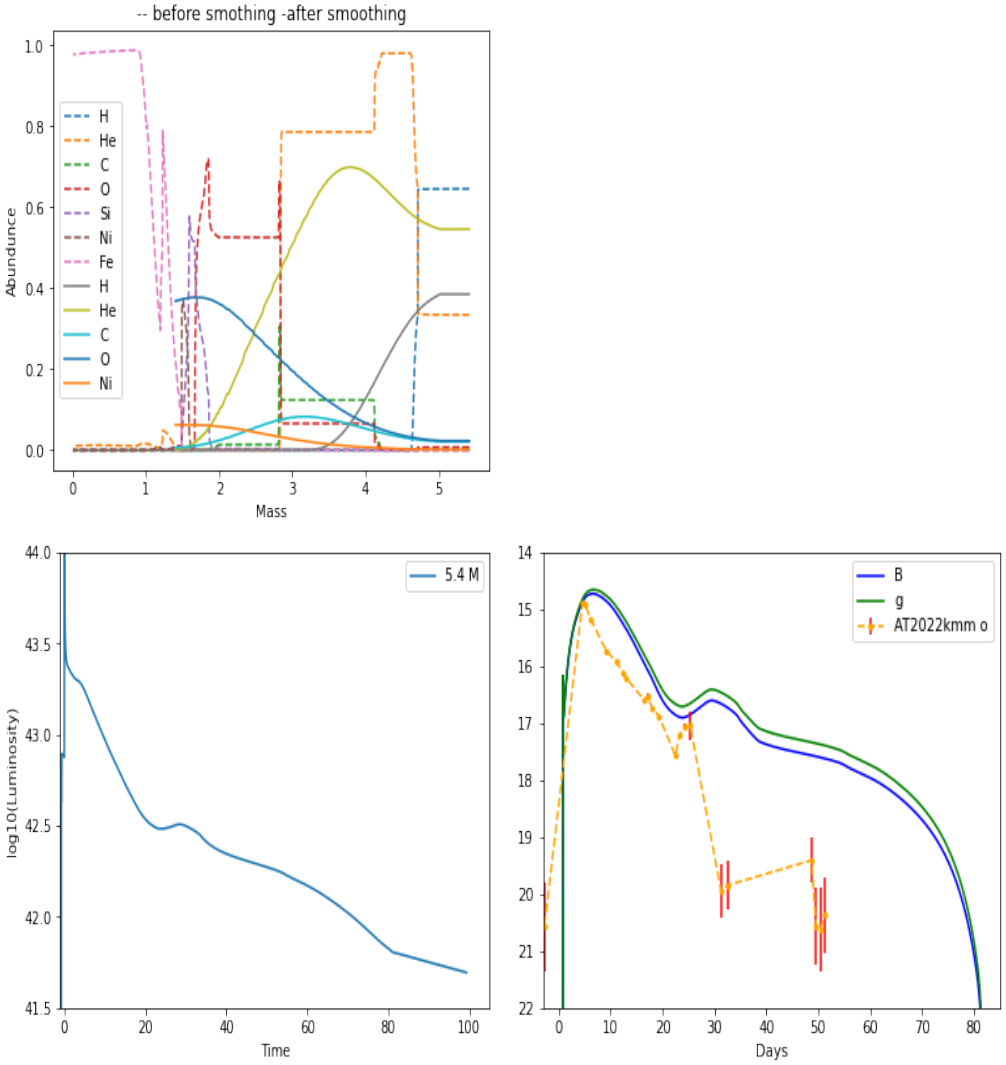

Figure 3.12: Figure shows MESA and SNEC outputs for progenitor with 15 $M_{\odot}$ ZAMS mass and mass loss leading to 5.4 $M_{\odot}$ prior to core-collapse. Top pre-explosion composition profile from MESA. Bottom left SNEC bolometric lightcurve. Bottom right Magnitudes in Bes B and SDSS g

The standard explosion fails to improve on the previous simulations
6) 5.4 $M_{\odot}$ star with lower amount of ^{56}Ni generated: 0.05 $M_{\odot}$

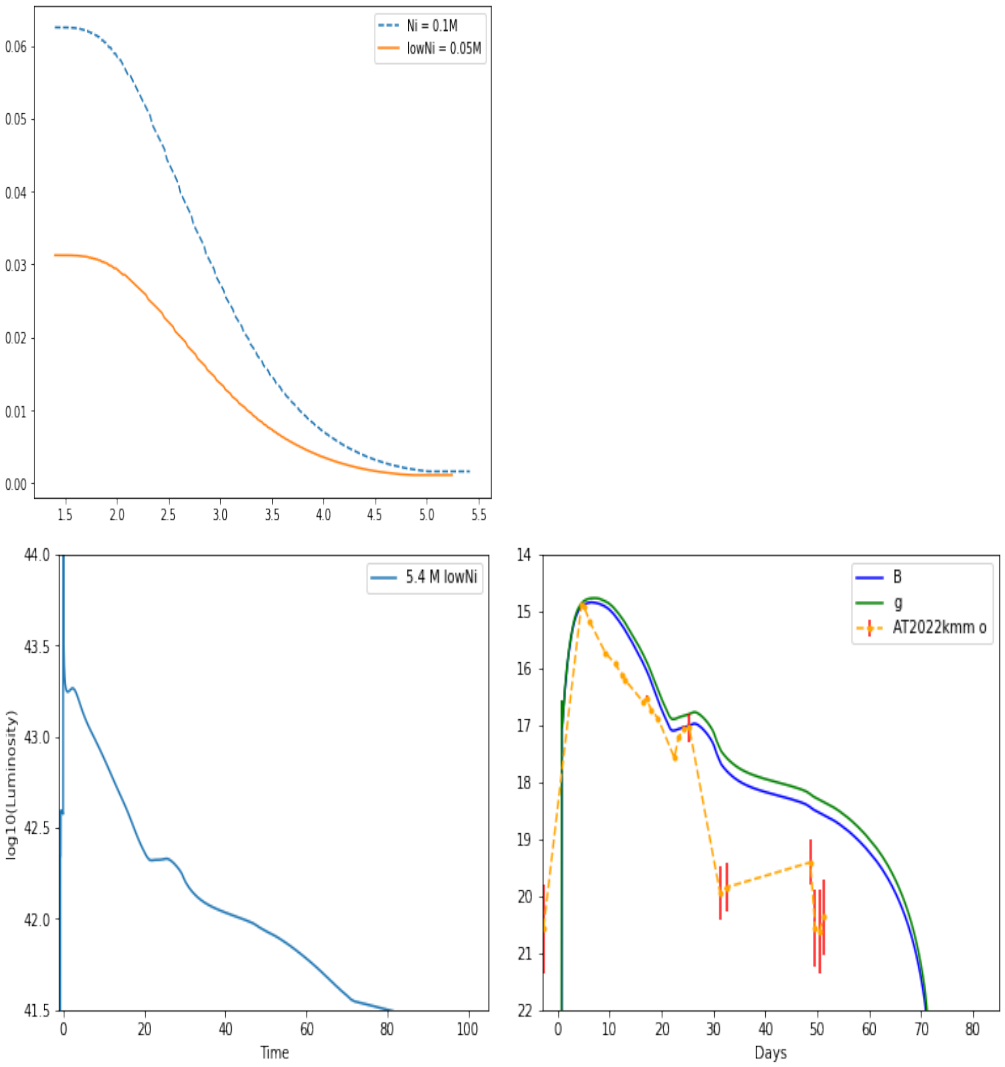

Figure 3.13: Figure shows MESA and SNEC outputs for progenitor with 15 $M_{\odot}$ ZAMS mass and mass loss leading to 5.4 $M_{\odot}$ prior to core-collapse exploded with half the amount of ^{56}Ni. Top pre-explosion ^{56}Ni profile from MESA. Bottom left SNEC bolometric lightcurve. Bottom right Magnitudes in Bes B and SDSS g

Lowering the ^{56}Ni mass improved the onset of re-brightening and the energy of re-brightening epoch $\sim 10^{48}$erg agrees better with the observation 7) 5.2 $M_{\odot}$ star, the star was evolved similar to 5.6 $M_{\odot}$ star and `wind_H_envelope_limit` was set to 0.5 $M_{\odot}$ that limited the hydrogen envelope to 0.5 $M_{\odot}$

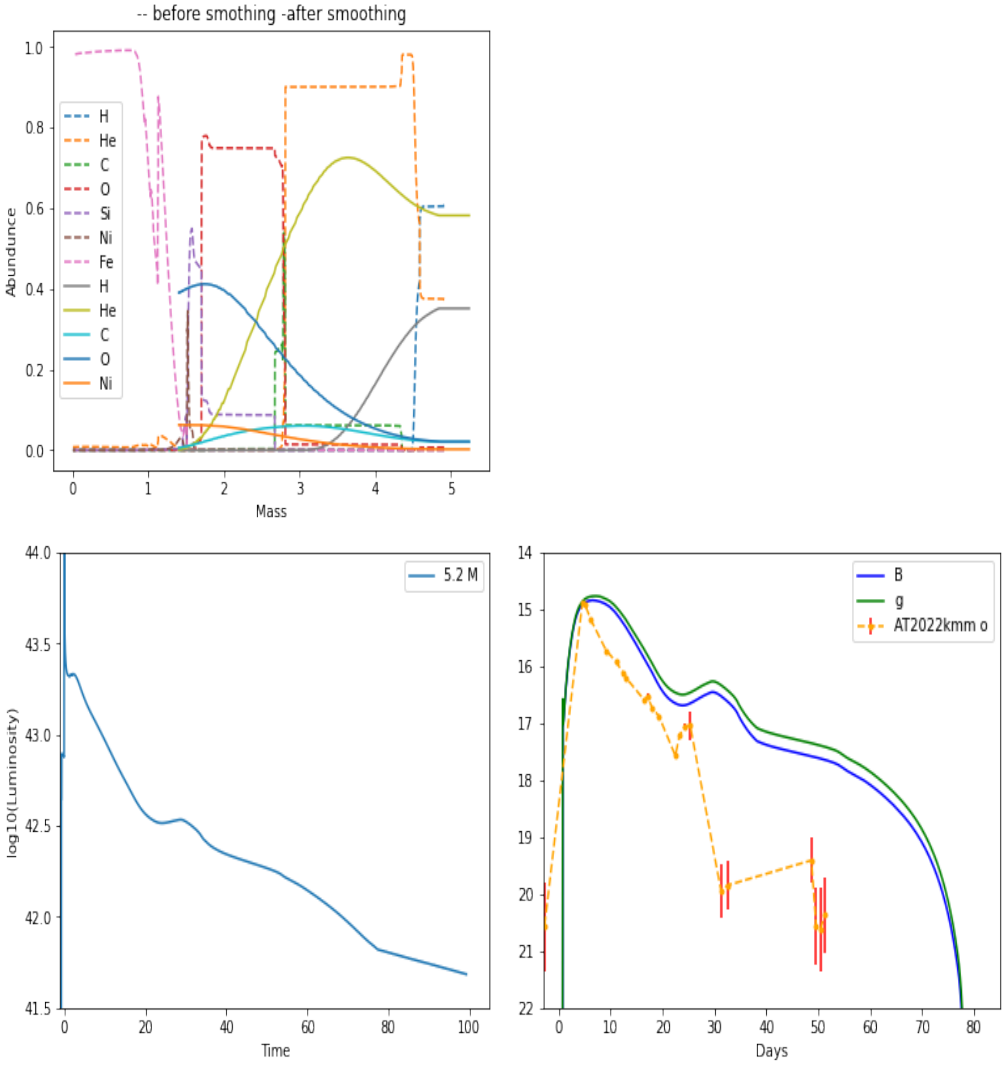

Figure 3.14: MESA and SNEC outputs for progenitor with 15 $M_{\odot}$ ZAMS mass and mass loss leading to 5.2 $M_{\odot}$ prior to core-collapse exploded. Top pre-explosion composition profile from MESA. Bottom left SNEC bolometric lightcurve. Bottom right Magnitudes in Bes B and SDSS g

The standard explosion had similar shortcoming as the standard explosion of 5.4 $M_{\odot}$ star

8) 5.2 $M_{\odot}$ pre-explosion progenitor star with lower amount of ^{56}Ni generated: 0.05 $M_{\odot}$

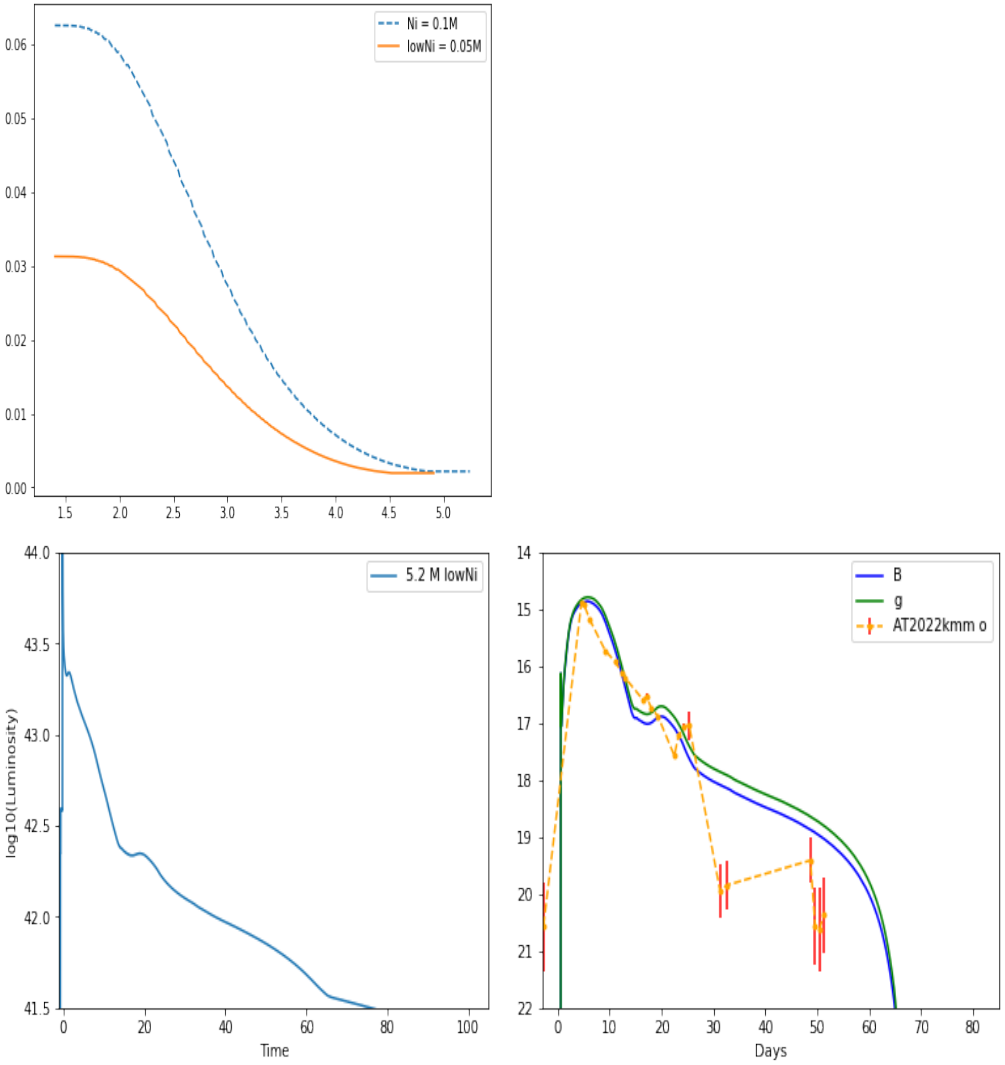

Figure 3.15: Figure shows MESA and SNEC outputs for progenitor with 15 $M_{\odot}$ ZAMS mass and mass loss leading to 5.2 $M_{\odot}$ prior to core-collapse exploded with half the amount of ^{56}Ni. Top pre-explosion ^{56}Ni profile from MESA. Bottom left SNEC bolometric lightcurve. Bottom right Magnitudes in Bes B and SDSS g

The depleted Hydrogen envelope generated a sharp rise and fall of desire, but the lower amount of background radioactive powering lead to an earlier re-brightening phase

9) 5.1 $M_{\odot}$ pre-explosion progenitor star, the star was evolved similar to 5.6 $M_{\odot}$ star and `wind_H_envelope _limit` was set to 0.4 $M_{\odot}$ that limited the hydrogen envelope to 0.4 $M_{\odot}$

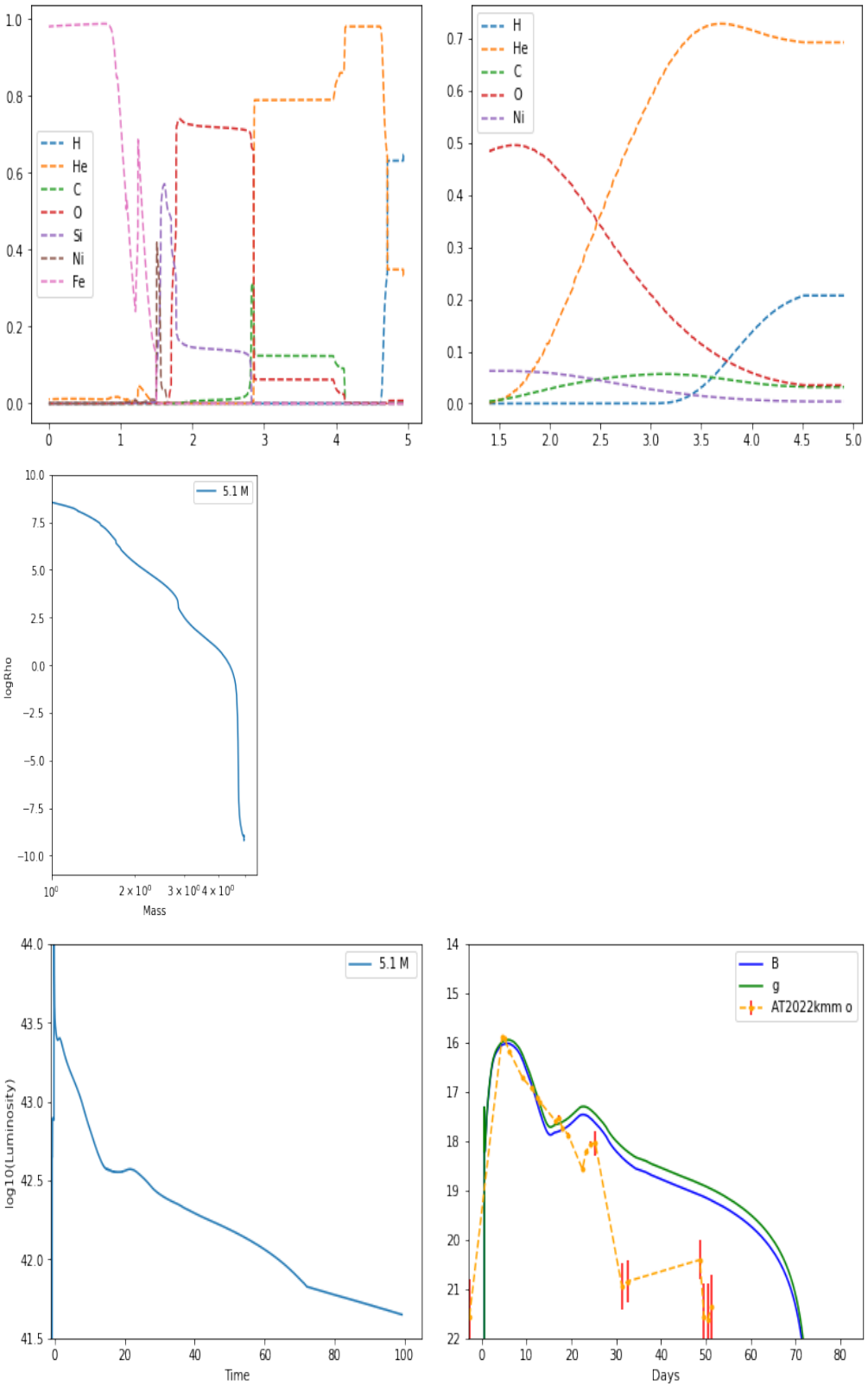

Figure 3.16: MESA and SNEC outputs for progenitor with 15 $M_{\odot}$ ZAMS mass and mass loss leading to 5.1 $M_{\odot}$ prior to core-collapse exploded. Top pre-explosion composition profile from MESA. Bottom left SNEC bolometric lightcurve. Bottom right Magnitudes in Bes B and SDSS g

The standard explosion shares the success and the failures of the modified 5.2 $M_{\odot}$ star explosion but the re-brightening phase lightcurve profile is a improved.
10) 5.1 $M_{\odot}$ pre-explosion progenitor star with lower amount of ^{56}Ni generated: 0.05 $M_{\odot}$ we that initial fall is too sharp and the late time luminosity profile is also not simulated.

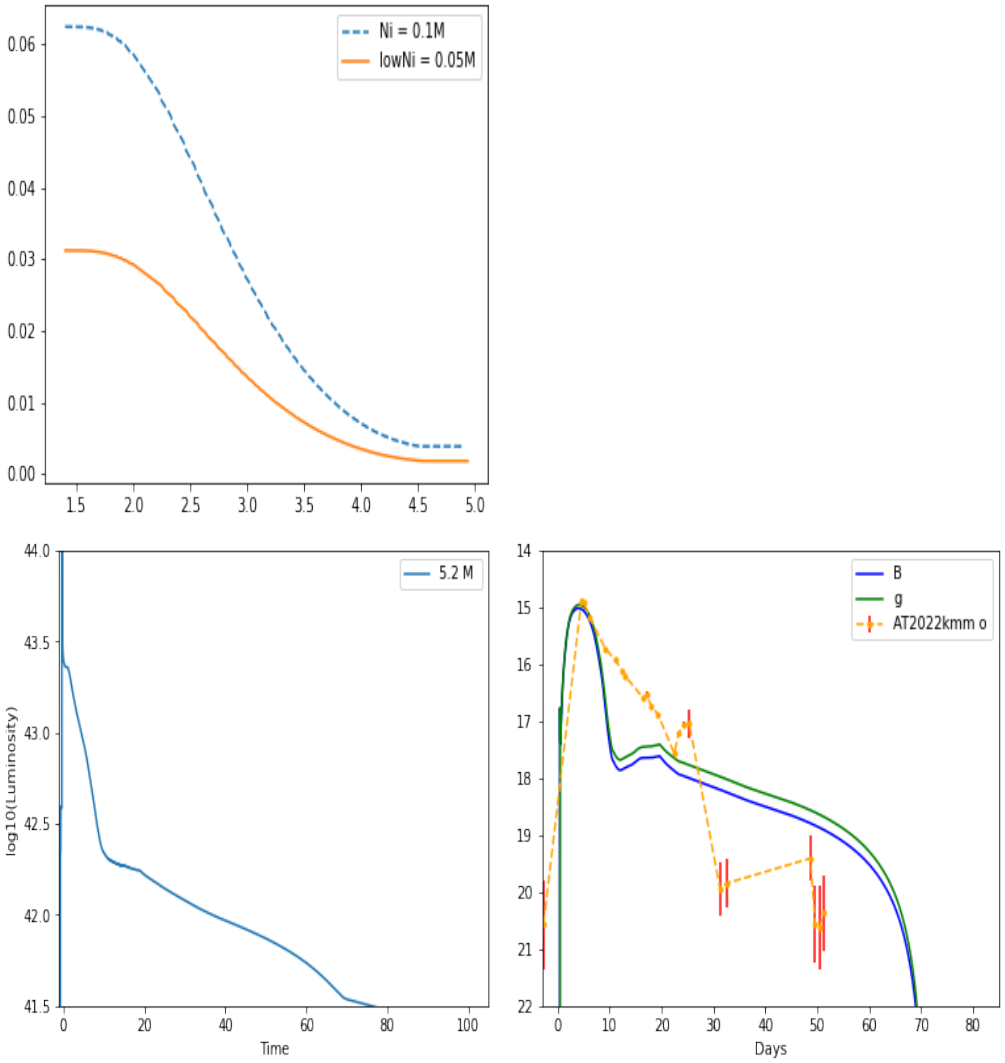

Figure 3.17: Figure shows MESA and SNEC outputs for progenitor with 15 $M_\odot$ ZAMS mass and mass loss leading to 5.1 $M_\odot$ prior to core-collapse exploded with half the amount of ^{56}Ni. (Top) pre-explosion ^{56}Ni profile from MESA. Bottom left SNEC bolometric lightcurve. Bottom right Magnitudes in Bes B and SDSS g

Next we distributed the ^{56}Ni differently i.e. more ^{56}Ni is dredged up and it is distributed throughout the star expecting the radioactive powering is altered as ^{56}Ni decay produces X-rays that end up escaping and not observed by the matetial in the ejecta
11) 5.1 $M_\odot$ star very low amount of ^{56}Ni is generated: 0.01 $M_\odot$ and its deposited outside of the 1.4$M_\odot$ core and in the interior of 5 $M_\odot$(full star)

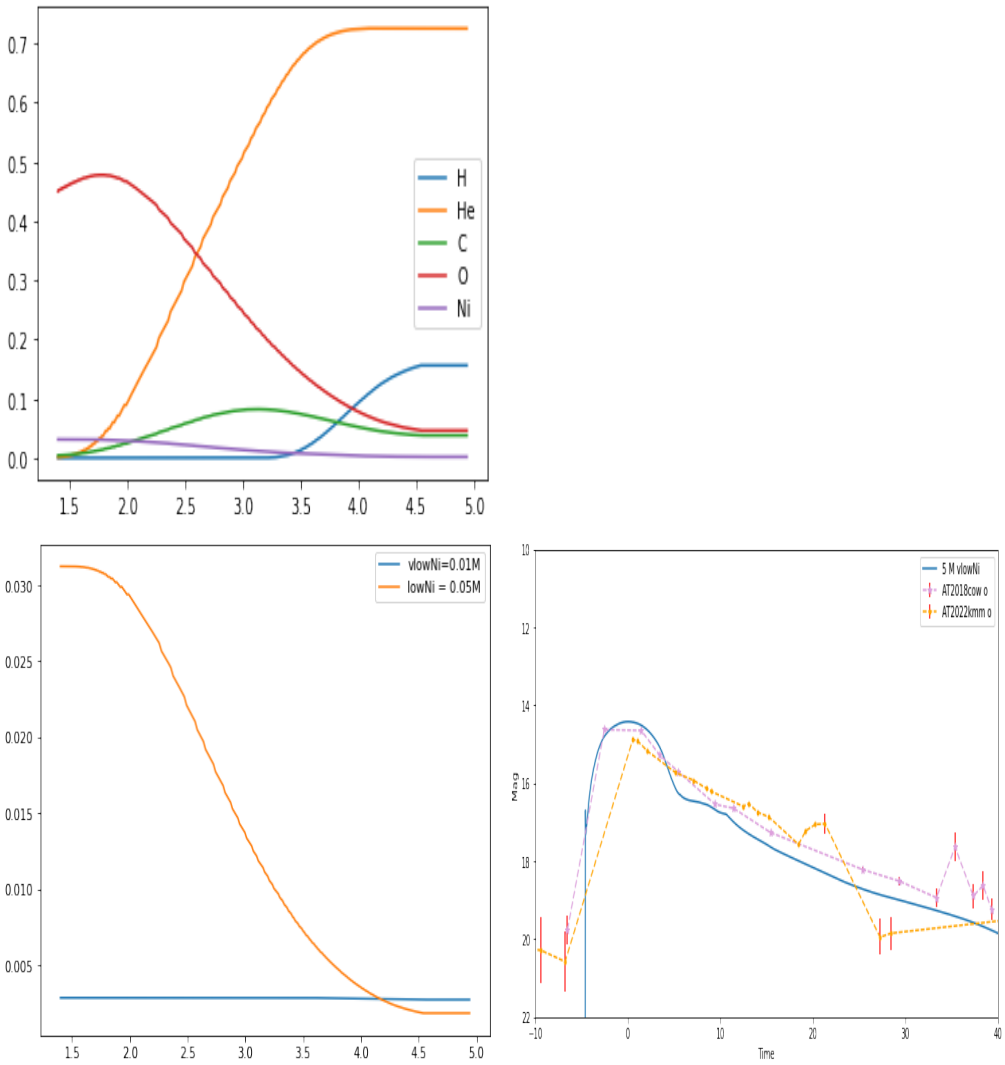

Figure 3.18: Figure shows MESA and SNEC outputs for progenitor with 15 $M_{\odot}$ ZAMS mass and mass loss leading to 5.1 $M_{\odot}$ prior to core-collapse exploded with very small amount of ^{56}Ni. Top pre-explosion composition profile abundance v mass from MESA. Bottom left ^{56}Ni profile. Bottom right Magnitudes

The initial rise and the fall of lightcurve matches well with observed light curves of the FBOTs.
This encouraged further modifications and simulation by altering the amount of ^{56}Ni generated and distributing it throughout the star

12) 5.1 $M_{\odot}$ pre-explosion progenitor star low amount of ^{56}Ni is generates:

$0.02M_{\odot}$ and $0.03M_{\odot}$

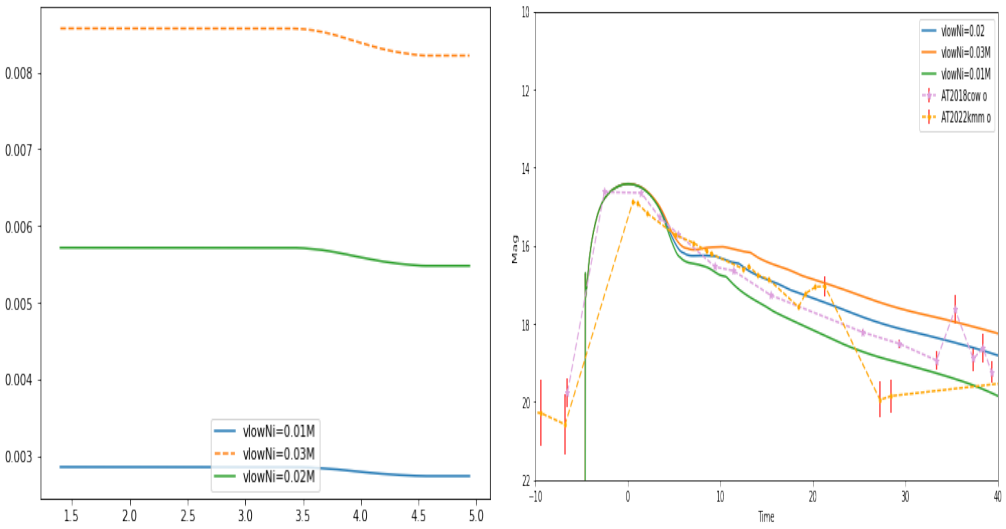

Figure 3.19: Figure shows MESA and SNEC outputs for progenitor with 15 $M_{\odot}$ ZAMS mass and mass loss leading to 5.1 $M_{\odot}$ prior to core-collapse exploded with varying amounts of ^{56}Ni. Left pre-explosion ^{56}Ni profile from MESA. Right Magnitudes

The model with $0.02M_{\odot}$ ^{56}Ni is the best approximation for the lightcurve profile of the FBOT, but these fail in reproducing the kink at the desired epoch.
It might be necessary to introduce a metal-rich cloud at $41 - 50$ AU.

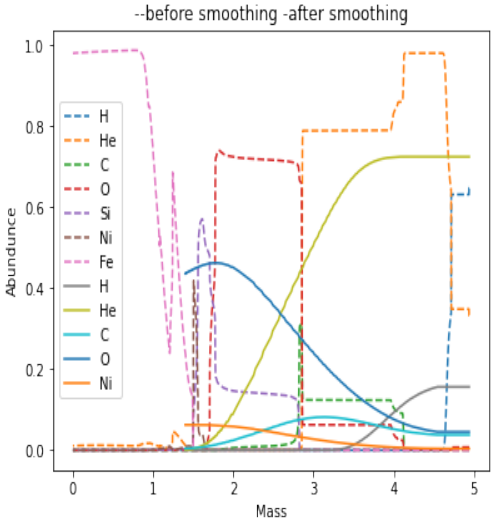

Figure 3.20: Figure shows MESA output for progenitor with 15 $M_{\odot}$ ZAMS mass and mass loss leading to 5 $M_{\odot}$ prior to core-collapse. Pre-explosion composition profile from MESA.

13) 5 $M_{\odot}$ pre-explosion progenitor stars, the star was evolved similar to 5.6 $M_{\odot}$ star and wind_H_envelope _limit was set to 0.3 $M_{\odot}$ that limited the hydrogen envelope to 0.3 $M_{\odot}$
Various SNEC simulations: standard and multiple modified explosions were performed on 5 $M_{\odot}$ star

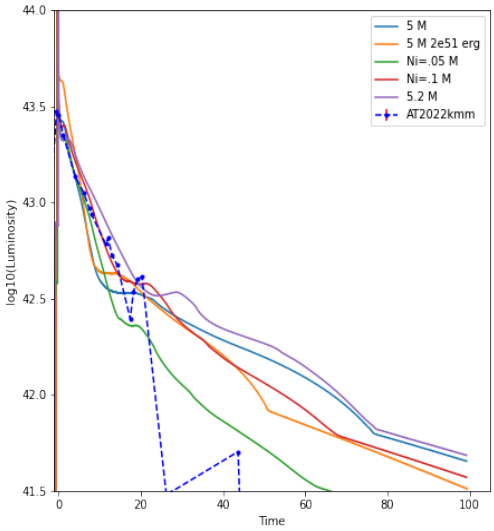

The low amount of Hydrogen was better suited for obtaining the initial rise and fall and 0.1$M_{\odot}$ ^{56}Ni distributed in outer layer improved the profile of re-brightening epoch but all fail in post re-brightening fall in brightness

In the following runs multiple metal rich layers from the interior of the star were removed

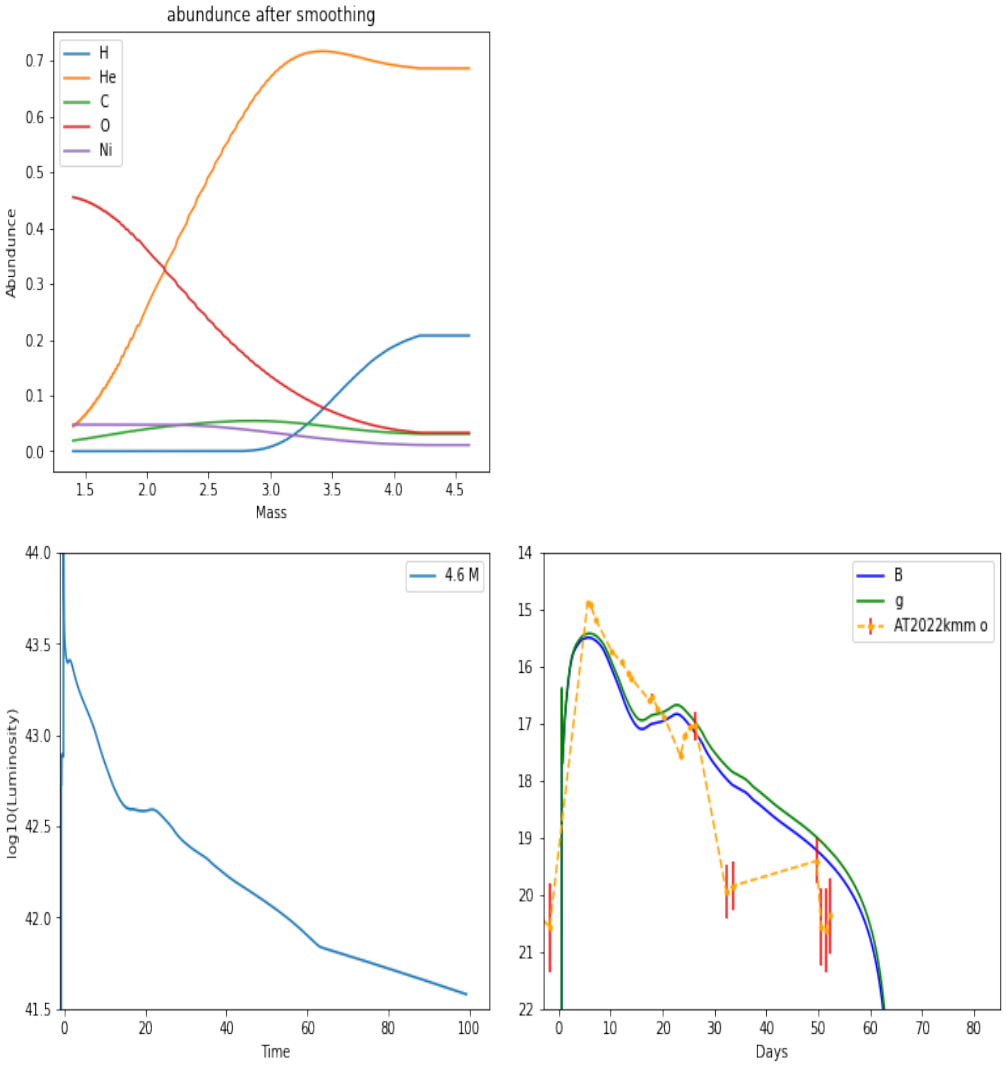

Figure 3.21: Figure shows MESA and SNEC outputs for progenitor with 15 $M_{\odot}$ ZAMS mass and mass loss and 0.3 $M_{\odot}$ metal removal leading to 4.6 $M_{\odot}$ prior to core-collapse. Top pre-explosion composition profile from MESA. Bottom left SNEC bolometric lightcurve. Bottom right Magnitudes in Bes B and SDSS g

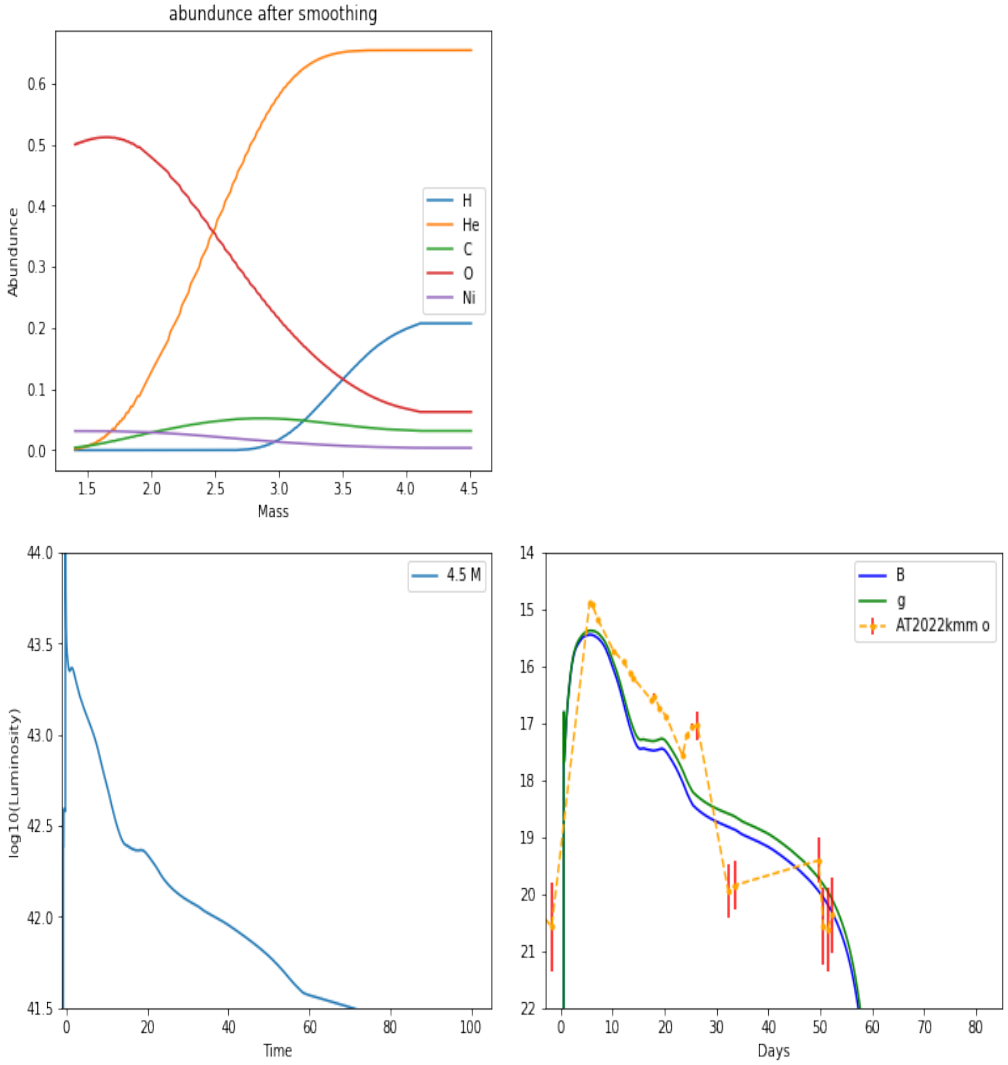

Figure 3.22: Figure shows MESA and SNEC outputs for progenitor with 15 $M_{\odot}$ ZAMS mass and mass loss and 0.4 $M_{\odot}$ metal removal leading to 4.5 $M_{\odot}$ prior to core-collapse. Top pre-explosion composition profile from MESA. Bottom left SNEC bolometric lightcurve. Bottom right Magnitudes in Bes B and SDSS g

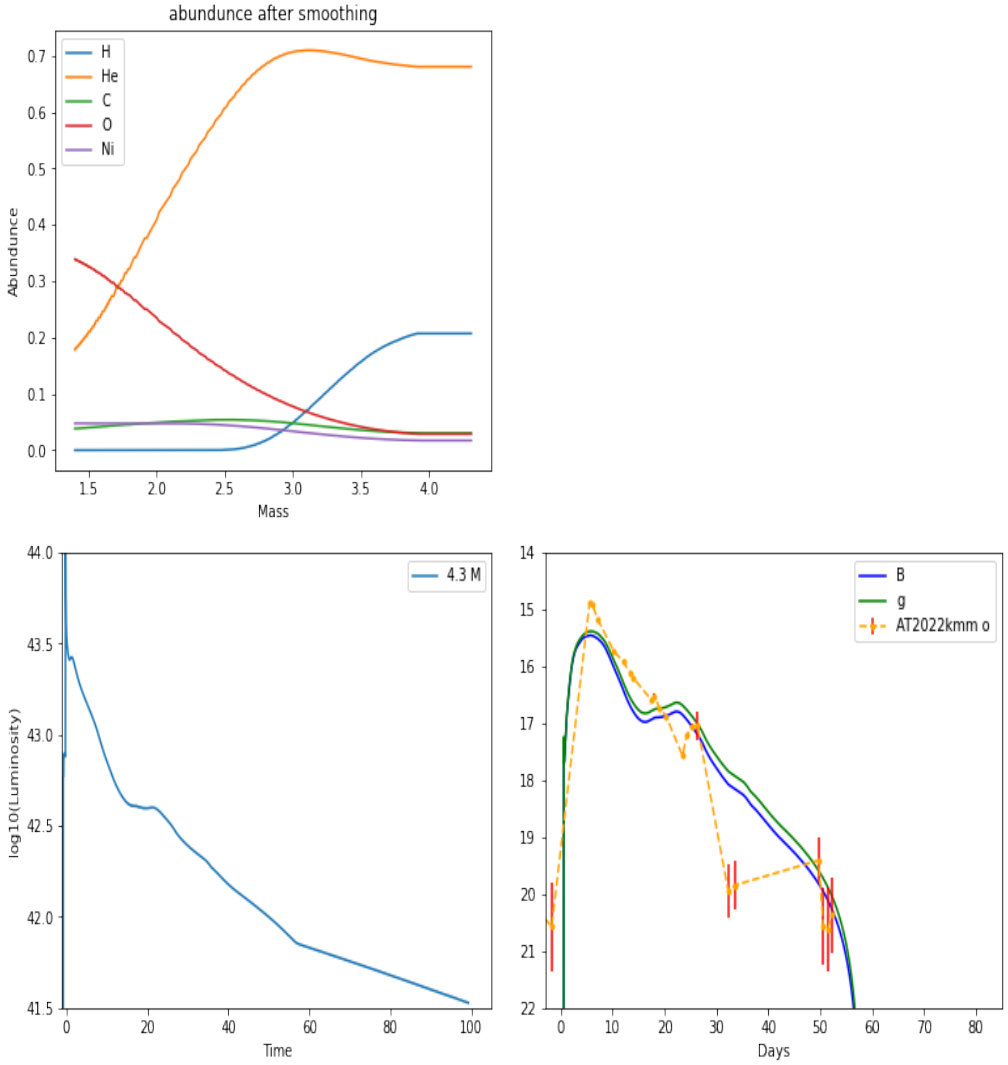

Figure 3.23: Figure shows MESA and SNEC outputs for progenitor with 15 $M_\odot$ ZAMS mass and mass loss and 0.6 $M_\odot$ metal removal leading to 4.3 $M_\odot$ prior to core-collapse. Top pre-explosion composition profile from MESA. Bottom left SNEC bolometric lightcurve. Bottom right Magnitudes in Bes B and SDSS g)

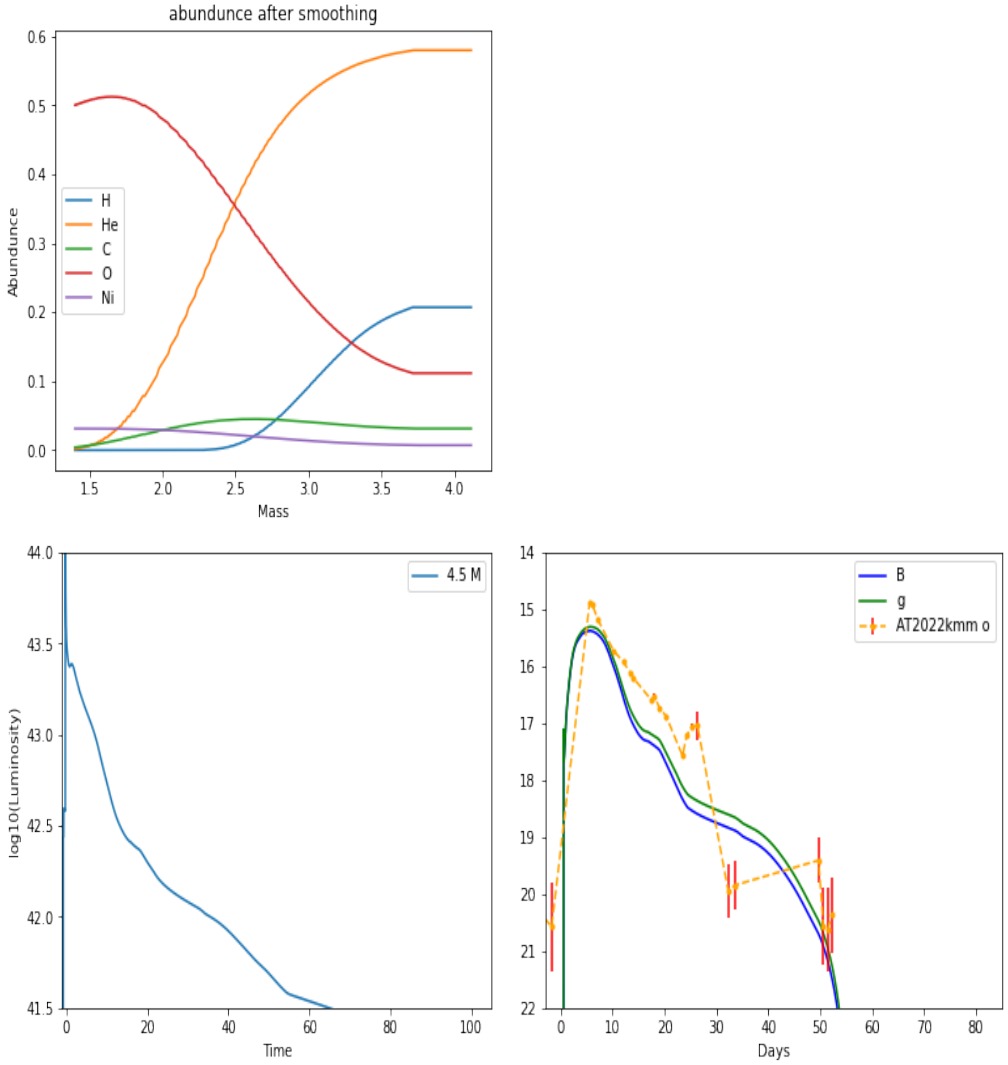

Figure 3.24: Figure shows MESA and SNEC outputs for progenitor with 15 $M_{\odot}$ ZAMS mass and mass loss and 0.8 $M_{\odot}$ metal removal leading to 4.1 $M_{\odot}$ prior to core-collapse. Top pre-explosion composition profile from MESA. Bottom left SNEC bolometric lightcurve. Bottom right Magnitudes in Bes B and SDSS g

Removal of metal-rich layers was better at replicating the rapid fall in the luminosity and generated a kink in all simulations but pre-re-brightening fall was not generated accurately.

To obtain the star profile without synthetic removal of the layers, MESA simultion of the star with ZAMS mass of 12 $M_{\odot}$ is evolved until core collapse, and during Helium burning mass loss is initiated until hydrogen envelope is

limited to 0.3 $M_{\odot}$.

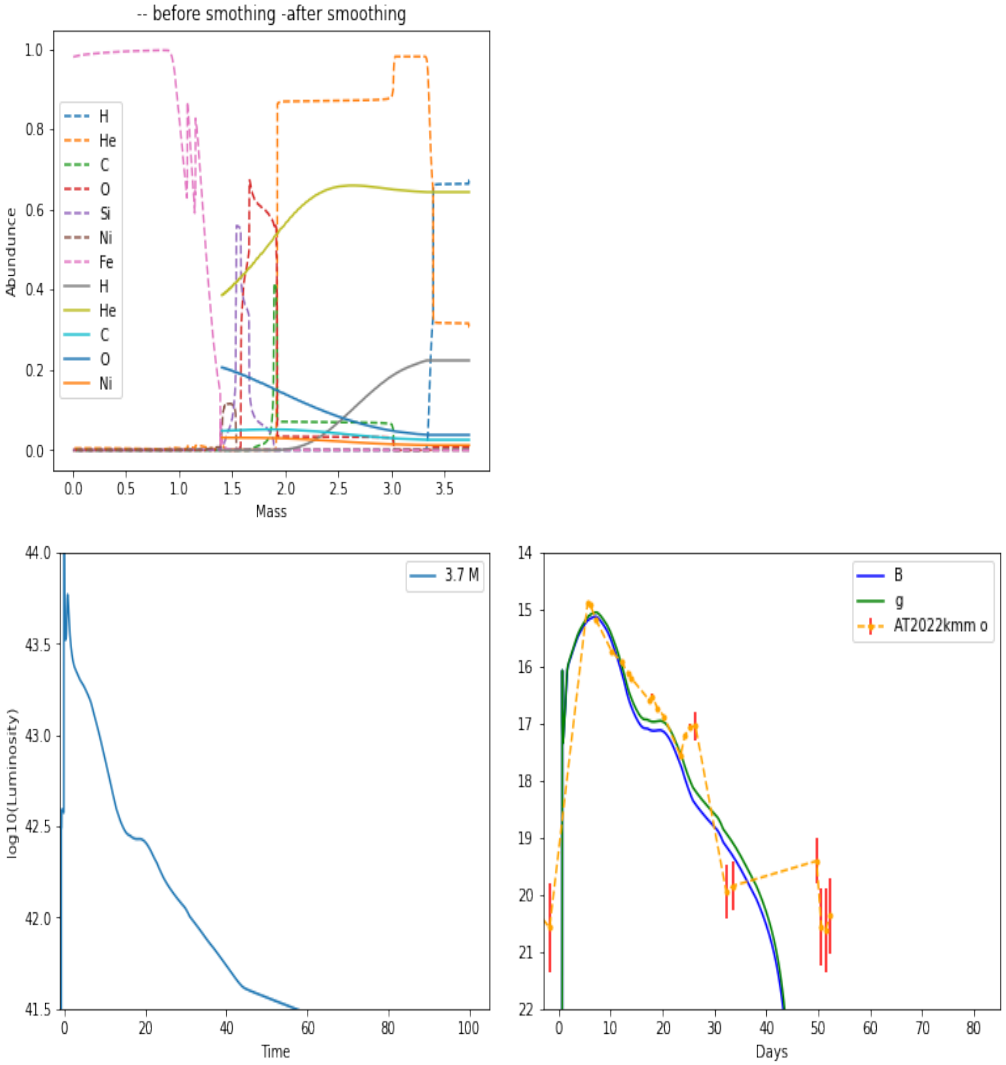

Figure 3.25: Figure shows MESA and SNEC outputs for progenitor with 12 $M_{\odot}$ ZAMS mass and mass loss leading to 3.7 $M_{\odot}$ prior to core-collapse. Top pre-explosion composition profile from MESA. Bottom left SNEC bolometric lightcurve. Bottom right Magnitudes in Bes B and SDSS g

Model parameters that could successfully obtain the re-brightening at the desired epoch were unsuccessful in reproducing the fall profile. 5.1 $M_{\odot}$ star model with a low amount of ^{56}Ni generated accurately fit the fall in brightness but failed to produce a significant re-brightening phase.

Simulations of PPISN with CSM interaction model:

We also explored the model of Circumstellar Interaction of a Pulsational Pair-instability Supernova for the Fast Blue Optical Transient AT2018Cow described by Shing-Chi Leung et.al., we focus on varying the mass and density profile of the circumstellar matter of 41 $M_{\odot}$ Helium star.
PPISN test case evolves a very massive helium star from He-ZAMS up to the onset of a pulsational pair-instability event. For our models, we started with a 55 $M_{\odot}$ Helium star and evolved it until significantly metal-rich inner shells are formed and at the time of PPISN only a 41.3 $M_{\odot}$ star remains. To this stellar structure we introduce the CSM of our desire, this stellar composition profile is then taken as input by SNEC. SNEC allows us to control the amount of ^{56}Ni generated and adjust the explosion energy.

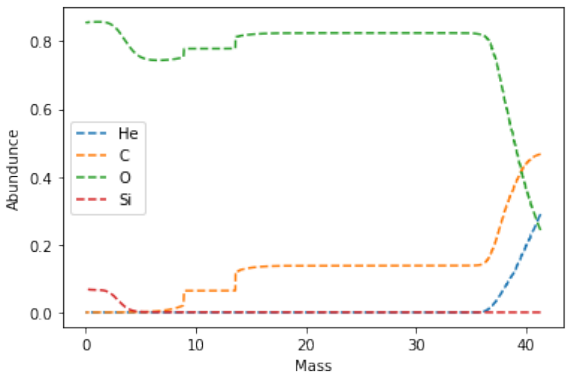

Figure 3.26: PPISN progenitor abundance profile

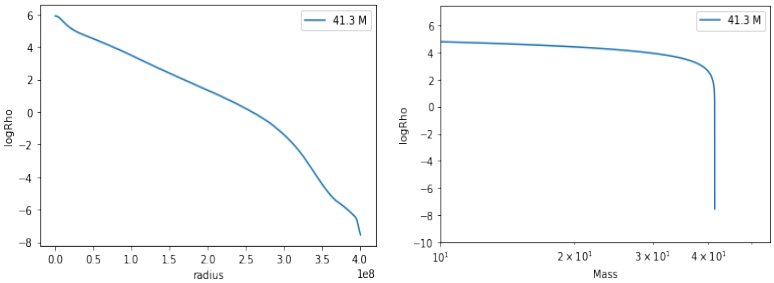

Figure 3.27: Density profile of progenitor

No.	Mass of CSM	Amount of ^{56}Ni	Density profile	Explosion Energy	fraction of Hydrogen in CSM	fraction of Helium in CSM	Figure
1	2	0.62	$\frac{1}{r}$	5×10^{51}	0	0.7	Figure 3.26
2	2	0.62	$\frac{1}{r^2}$	5×10^{51}	0	0.7	Figure 3.27
3	1	0.62	$\frac{1}{r}$	5×10^{51}	0	0.7	Figure 3.28
4	1	0.62	$\frac{1}{r^2}$	5×10^{51}	0	0.7	Figure 3.29
5	0.2	0.62	$\frac{1}{r^2}$	$5 \times 10^{50-51}$	0	0.7	Figure 3.31
6	0.1,0.2 n 0.5	0.62	$\frac{1}{r^2}$	5×10^{51}	0	0.7	Figure 3.32
7	0.1,0.2 n 0.5	0.52	$\frac{1}{r^2}$	5×10^{51}	0	0.7	Figure 3.33
8	0.2	0.52	$\frac{1}{r}$	5×10^{51}	0,0.5 n 0.98	0.7, 0.35 n 0.01	Figure 3.34
9	0.2	0.52	$\frac{1}{r^2}$	5×10^{51}	0,0.5 n 0.98	0.7, 0.35 n 0.01	Figure 3.35
10	0.3	0.52	$\frac{1}{r}$	5×10^{51}	0,0.5 n 0.98	0.7, 0.35 n 0.01	Figure 3.36
11	0.3	0.52	$\frac{1}{r^2}$	5×10^{51}	0,0.5 n 0.98	0.7, 0.35 n 0.01	Figure 3.37

Table 3.3: Explosion parameters for PPISN CSM interaction model

1) Helium medium of 2 $M_\odot$ extending upto 10^{14}cm with 1/r density profile is added to the Star, 0.62 $M_\odot$ is the amount of ^{56}Ni and explosion energy is set at $5{\times}10^{51}$ erg

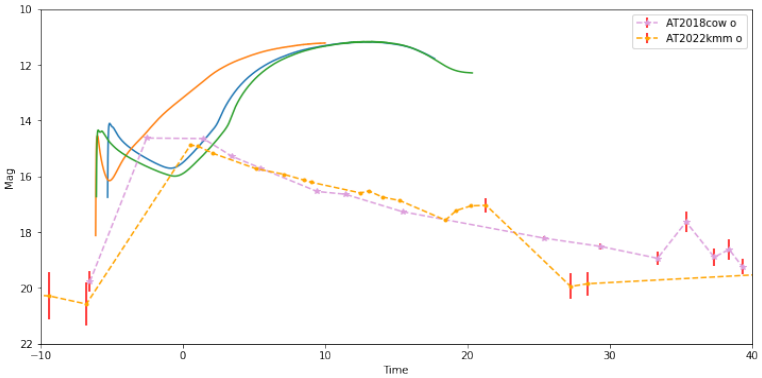

Figure 3.28: SNEC output for PPISN progenitor with $2M_{\odot}$ CSM with 1/r density profile

2) Helium medium of 2 $M_{\odot}$ extending upto 10^{14}cm with $1/r^2$ density profile is added to the Star, 0.62 $M_{\odot}$ is the amount of ^{56}Ni and explosion energy is set at 5×10^{51} erg

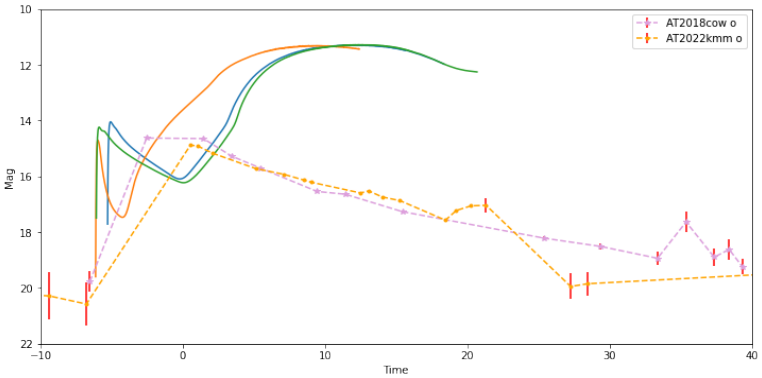

Figure 3.29: SNEC output for PPISN progenitor with $2M_{\odot}$ CSM with $1/r^2$ density profile

3) Helium medium of 1 $M_{\odot}$ extending upto 10^{14}cm with 1/r density profile is added to the Star, 0.62 $M_{\odot}$ is the amount of ^{56}Ni and explosion energy is set at 5e51 erg

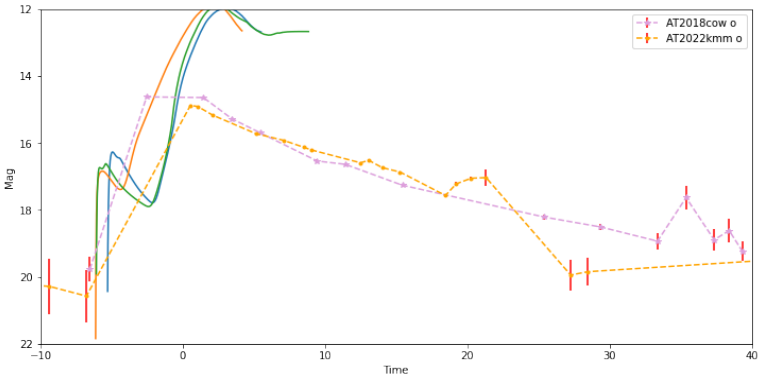

Figure 3.30: SNEC output for PPISN progenitor with $1M_{\odot}$ CSM with 1/r density profile

4) Helium medium of 1 $M_{\odot}$ extending upto 10^{14}cm with $1/r^2$ density profile is added to the Star, 0.62 $M_{\odot}$ is the amount of ^{56}Ni and explosion energy is set at 5e51 erg

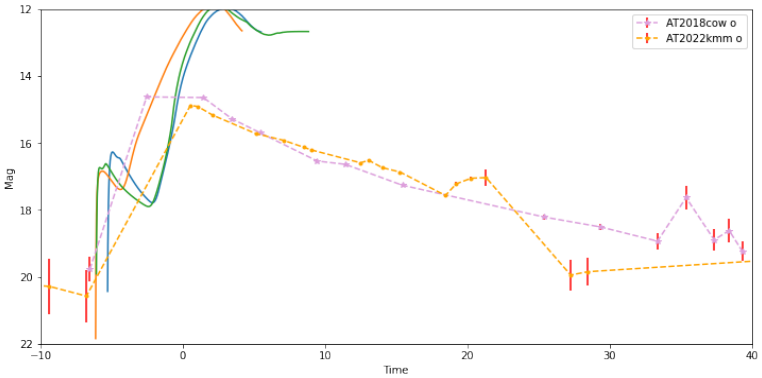

Figure 3.31: SNEC output for PPISN progenitor with $1M_{\odot}$ CSM with $1/r^2$ density profile

The large amount of mass in the CSM produced light curves that deviated from the observations drastically, we explored explosions with lower CSM mass
0.2 $M_{\odot}$ csm outside the star distribution 1/r vs $1/r^2$

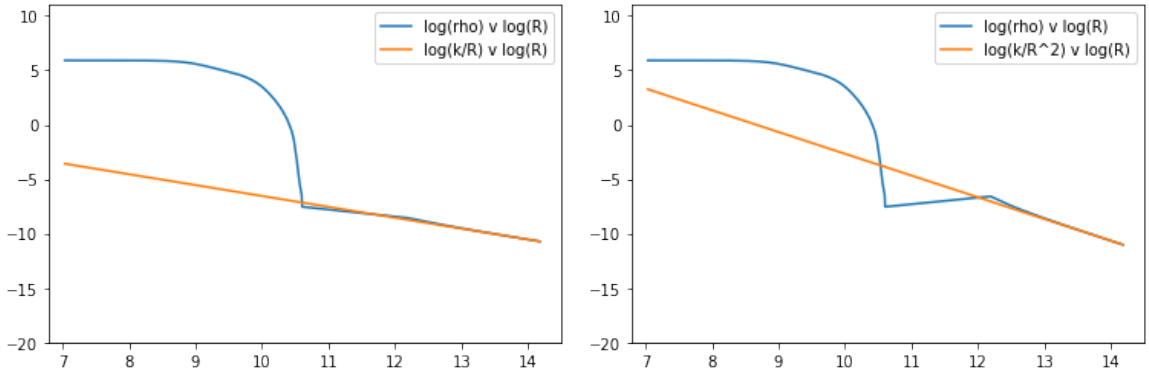

Figure 3.32: Extended envelop density profile

5) Helium medium of 0.2 $M_{\odot}$ extending upto 10^{14}cm with $1/r^2$ density profile is exploded with energy of 5×10^{50} vs 5×10^{51}

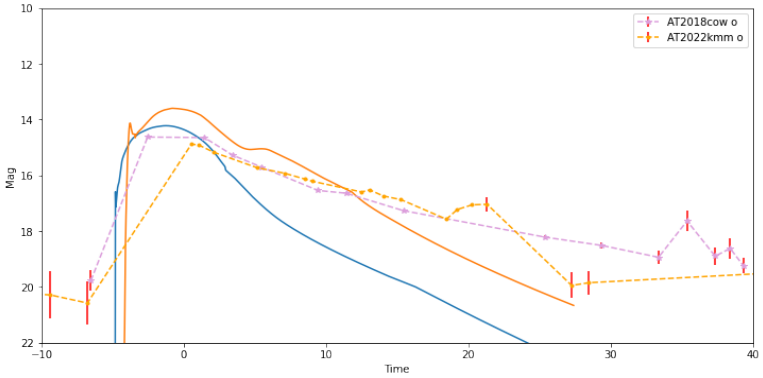

Figure 3.33: comparing SNEC outputs for PPISN progenitor with $0.2M_{\odot}$ CSM with $1/r^2$ density profile exploded with different energies

6) comparing light curves of 0.1 $M_{\odot}$, 0.2 $M_{\odot}$, 0.5 $M_{\odot}$ of extended Helium medium

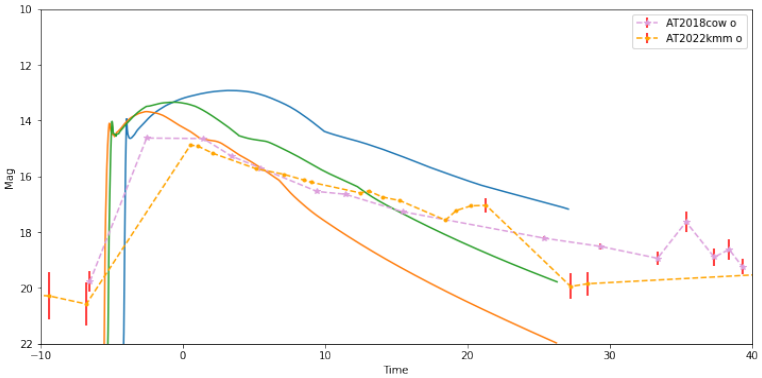

Figure 3.34: comparing SNEC outputs for PPISN progenitor with 0.1,0.2,$0.5 M_{\odot}$ CSM

7) Ni amount changed to 0.52 from $0.62 M_{\odot}$, light curves with 0.1,0.2,$0.5 M_{\odot}$ Helium medium with exlosion energy of 5×10^{51} erg

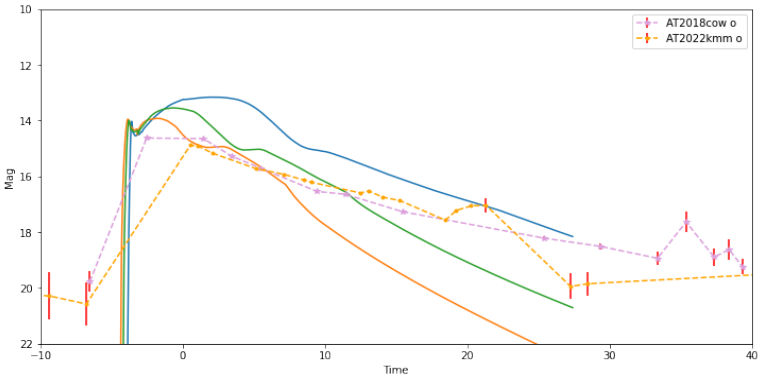

Figure 3.35: comparing SNEC outputs for PPISN progenitor with 0.1,0.2,$0.5 M_{\odot}$ CSM

8) varying the composition of 0.2 $M_{\odot}$ medium from no Hydrogen to full 0.2 $M_{\odot}$ Hydrogen

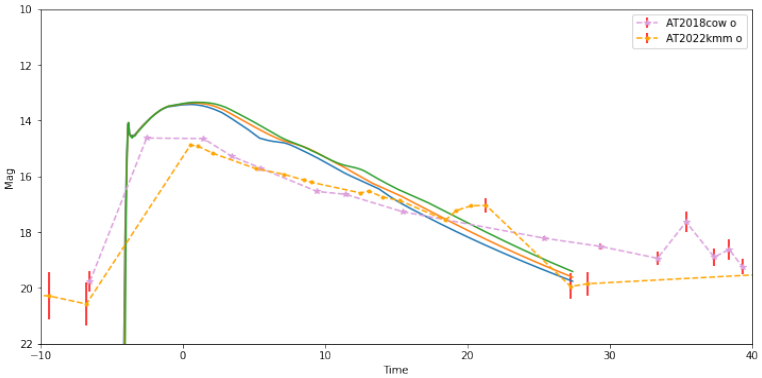

Figure 3.36: comparing SNEC outputs for PPISN progenitor with $0.2M_{\odot}$ CSM 1/r density profile with different H abundances

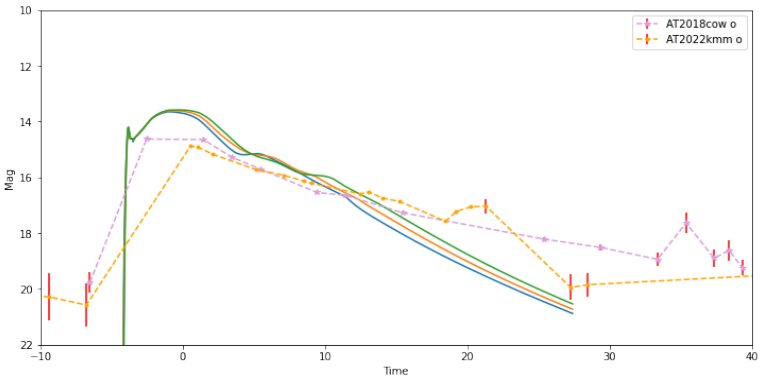

Figure 3.37: comparing SNEC outputs for PPISN progenitor with $0.2M_{\odot}$ CSM $1/r^2$ density profile with different H abundances

11) varying the composition of 0.3 $M_{\odot}$ medium from no Hydrogen to full 0.3 $M_{\odot}$ Hydrogen

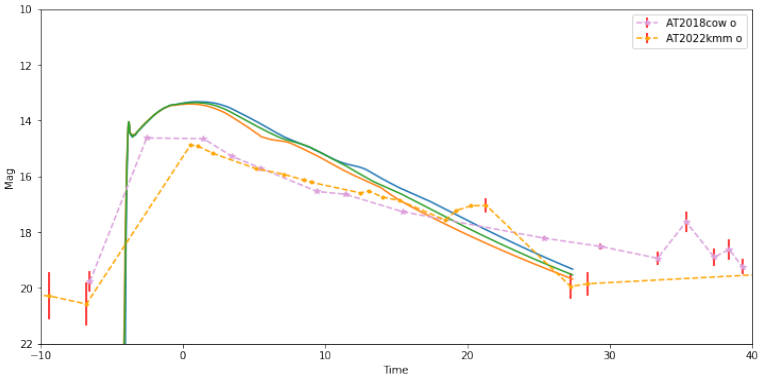

Figure 3.38: comparing SNEC outputs for PPISN progenitor with $0.3M_{\odot}$ CSM 1/r density profile with different H abundances

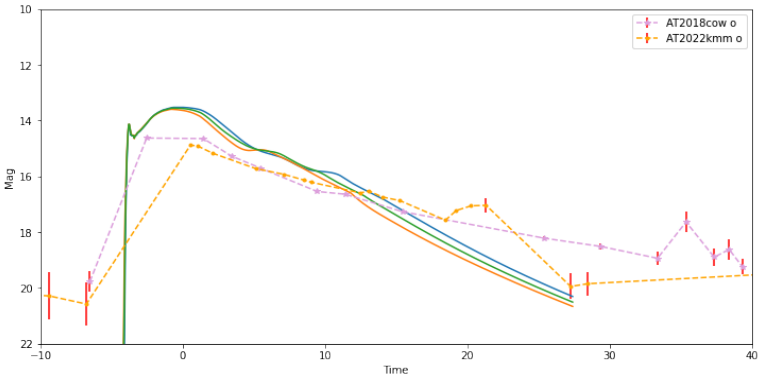

Figure 3.39: comparing SNEC outputs for PPISN progenitor with $0.3M_{\odot}$ CSM $1/r^2$ density profile with different H abundances

The small "knee" or "bump" feature is due to the additional luminosity input from exposed metal ions recapturing electrons as the photosphere cools and thins down, the metal ions in this case are the radioactive ^{56}Ni and 56Co i.e. Iron group

Mode with 0.2 $M_{\odot}$ Helium medium with $1/r^2$ density profile interacting with PPISN is successful in obtaining the rise and fall profile of the light curve but fails to generate the re-brightening.
To account for this it might be necessary to involve some metal-rich dense cloud at $41 - 50$ AU. The recombination of electrons and ions during the cooling of the material, thats heated up by the shock passing through it, would release the energy thats observed as rebrightening

Chapter 4

Summary

4.1 What did I learn?

My thesis focuses on studying a rare subclass of supernovae known as Fast Blue Optical Transients (FBOTs). Despite being scarcely investigated, FBOTs hold significant importance. Throughout my research, I gained a comprehensive understanding of supernova theory and the fundamental aspects of supernova classification.

To conduct my analysis, I performed data extraction and conducted photometric and spectral analyses using observations obtained from the Himalayan Chandra Telescope (HCT). I utilized various datasets, including the ATLAS Forced Photometry, ZTF Bright Transient Survey database, and NASA/IPAC Extragalactic Database, to study the FBOT labeled AT 2022kmm.

During the analysis, I extensively employed tools available in the Astropy project, enabling me to manipulate and interpret the data effectively. By comparing the lightcurve and spectral features, strong evidence emerged suggesting that AT 2022kmm is a FBOT similar to AT2018cow, a well-studied FBOT.

In addition to utilizing Astropy, I also acquired proficiency in employing SNID and Astrodash for further analysis and comparison of supernova characteristics.

To gain deeper insights into the properties of AT 2022kmm and explore possible theoretical models, I modeled its light curve using SNEC. To generate progenitor profiles and narrow down the parameter space of proposed models, I utilized MESA. Consequently, this allowed for a more accurate representation and interpretation of the observed data.

In summary, my research journey encompassed a thorough understanding of FBOTs, practical experience with data analysis tools such as Astropy, SNID, and Astrodash, and the application of modeling techniques using SNEC and MESA to study the specific case of AT 2022kmm.